Long-Term Observations of Galactic Cosmic Ray LET Spectra in Lunar Orbit by LRO/CRaTER

M. D. Looper[1], J. E. Mazur[1], J. B. Blake[1], H. E. Spence[2], N. A Schwadron[2], J. K. Wilson[2], A. P. Jordan[2], C. Zeitlin[3], A. W. Case[4], J. C. Kasper[5], L. W. Townsend[6], and T. J. Stubbs[7]

[1]The Aerospace Corporation, El Segundo, CA 90245, USA.

[2]University of New Hampshire, Durham, NH 03824, USA.

[3]Leidos Innovations Corporation, Houston, TX 77042, USA.

[4]Harvard-Smithsonian Center for Astrophysics, Cambridge, MA 02138, USA.

[5]University of Michigan, Ann Arbor, MI 48109, USA.

[6]University of Tennessee, Knoxville, TN 37996, USA.

[7]NASA Goddard Space Flight Center, Greenbelt, MD 20771, USA.

Corresponding author: Mark Looper (mark.d.looper@aero.org)

Key Points:

- The Cosmic Ray Telescope for the Effects of Radiation has measured galactic cosmic rays at the Moon over a full solar activity cycle.
- We have used the Geant4 radiation-transport code to improve background rejection in measurements of Linear Energy Transfer spectra.
- The intensity of galactic cosmic rays, as of early 2020, has recovered and now slightly exceeds the historically high levels of 2009.

This is the author manuscript accepted for publication and has undergone full peer review but has not been through the copyediting, typesetting, pagination and proofreading process, which may lead to differences between this version and the Version of Record. Please cite this article as doi: 10.1029/2020SW002543

Abstract

The Cosmic Ray Telescope for the Effects of Radiation (CRaTER) has been orbiting the Moon since 2009 aboard the Lunar Reconnaissance Orbiter (LRO). From this vantage point, it samples the interplanetary energetic particle population outside the shielding of the Earth's magnetosphere. We report the sensor's observations of galactic cosmic rays (GCRs) over a complete solar activity cycle. CRaTER is designed primarily to measure not the spectra of primary GCR particles outside the sensor, but rather their effects on matter, and in particular it measures the linear energy transfer (LET) or energy-deposit spectrum in its silicon detectors. We have used the Geant4 radiation-transport code to devise a background-rejection algorithm to improve these measurements of LET under 9.9 g/cm^2 of shielding, and the resulting observations show the changing radiation effects of GCRs as their intensity and spectrum vary with solar modulation. As of 2020 this intensity, after declining during solar maximum activity, has recovered to a level that exceeds by a few percent the historically high values seen during the deep solar minimum at the start of the LRO mission in 2009.

Plain Language Summary

Energetic particle radiation consists of fast-moving atomic fragments traveling in space. The particles with the highest energy, called cosmic rays, can penetrate even thick shielding and deposit their energy into astronauts or electronics, causing radiation damage. A sensor aboard the Lunar Reconnaissance Orbiter satellite has been measuring cosmic rays in orbit around the Moon since 2009, monitoring the varying intensity of their radiation effects, and this paper reports improvements we have made to these measurements. The Sun's output of energetic particles, magnetic fields, etc., varies on an 11-year cycle, and this activity affects the intensity of cosmic rays coming into the solar system. Our measurements of cosmic-ray radiation effects show that, after a decline during the middle of the solar activity cycle, as of 2020 their intensity has risen back to exceed the historically high levels seen at the start of the mission.

1 Introduction

1.1 CRaTER Observations of Galactic Cosmic Rays

The Cosmic Ray Telescope for the Effects of Radiation (CRaTER) has been measuring energetic particle radiation in orbit around the Moon aboard the Lunar Reconnaissance Orbiter (LRO) since mid-2009. Its sensor head consists of six circular silicon solid-state detectors arranged in three pairs, with one thick and one thin detector in each pair. The thick (1 mm) detectors have low energy-deposit thresholds and high gains so as to measure particles with low LET (linear energy transfer, the amount of energy lost by a particle per unit pathlength through a target), while the thin (nominally 150 μm) detectors have high thresholds and low gains so as to measure high-LET particles that will deposit enough energy to saturate the thick detectors' pulse-height analysis circuitry.

Unlike many spaceborne charged-particle telescopes, CRaTER is not primarily designed to measure the particle environment outside the sensor, though it has been used for that purpose (e.g., Wilson et al., 2019, Zeitlin et al., 2019, and references cited therein). Rather, it is designed to measure the effects of that environment on radiation-sensitive targets like spaceborne humans or electronics. To that end, between each of the adjacent pairs of detectors is placed a cylinder of A-150 tissue-equivalent plastic (TEP; Smathers et al., 1977) to approximate the shielding effects

of astronauts' soft tissue. The diagrams inset in each panel of Figure 1 represent the layout of detectors (yellow) and TEP (red); details are given by Spence et al. (2010). The detectors are numbered D1 to D6 from left to right in these sketches, with the odd-numbered detectors being thin and the even-numbered detectors being thick.

In the nominal attitude of the LRO spacecraft, with its imaging instruments pointing toward the nadir, the axis of the CRaTER sensor head points from zenith to nadir, with D1 facing space and D6 facing the lunar surface. Pulse-height analysis is carried out for all particle events depositing energy above the discriminator thresholds of one or more detectors, but for this study we analyze particle events that trigger all three thick detectors (D2, D4, D6) in coincidence, with measurement of the energy deposit at the nadir end of the stack being taken over by D5 for events where D6 saturates. This coincidence requirement nominally restricts consideration to particles entering the sensor within either end of the double-ended acceptance cone defined by detectors D2 and D6, which are 3.5 cm in diameter and 12 cm apart.

Most of the "albedo" charged particles coming up from the lunar surface do not have enough energy to go all the way through the CRaTER stack from D6 to D2 (Looper et al., 2013); thus for D2/D4/D6 coincidences the Moon acts as a beam stop, and the measurement should comprise a sample only of cosmic rays entering from space in the acceptance cone through the D1 aperture. These particles will be collimated within a cone of half-angle 16° around the boresight direction, and so all such particles penetrating a given detector should have the same pathlength within a few percent, allowing a consistent estimate of the particles' LET spectrum to be obtained by dividing the energy deposit spectrum by the detector thickness.

Actually, according to the definitions of the International Commission on Radiological Protection (ICRP, 1991), the term "linear energy transfer" refers to the energy *lost* by the *particle* in traversing matter, whereas detectors like those of CRaTER measure the energy *absorbed* by the *target*. This quantity divided by the mean pathlength through the detector, called "lineal energy" and denoted "y," will be equal to the "unrestricted LET" if the detector is thick enough to recapture the energy carried away from the primary particle by all secondary electrons; Looper et al. (2013) showed the effects of energy lost to escaping secondaries in the different CRaTER detectors. The "restricted LET" is the energy lost by the particle per unit pathlength, with the exception of the quantity carried away by secondary electrons above a given energy. As such, it will be numerically closer to the lineal energy if the cutoff energy is chosen appropriately to ignore electrons that will escape from the target detectors, although it remains a measure of the energy lost by the particle rather than of that absorbed by the target. However, the three quantities unrestricted LET, restricted LET, and lineal energy are numerically close to one another in these measurements, and in discussions of the space environment they are often referred to under the umbrella of the single term "LET," as in the title of this paper. To emphasize that we are presenting observations by physical detectors (and simulations of those observations) in the figures of this paper, rather than abstracted properties of the particles and target materials, plots will be presented in terms of "normalized energy deposit," which is simply the measured energy deposit in a detector divided by its thickness. This has the same units as LET and lineal energy, and is an estimate of both.

The CRaTER website (http://crater-web.sr.unh.edu) provides measurements of the LET spectrum of such particles in near real time. These measurements are scaled from the raw pulse-height spectra in each detector for all particle events that satisfy the above coincidence requirements, using the scaling algorithm developed by Case et al. (2013). Thus, the time

variation of these LET spectra includes a contribution from the time variation of any background signal in those measurements, as well as the actual time variation of the desired signal. While the scaling brings the overall amplitude of the spectrum to the correct level, variations in the background signal may mask variations in the foreground signal if the particles causing each are different and thus have different amplitudes of variation, as discussed in Section 2. The present work devises corrections using the individual detector pulse heights for each event so that we can reject, as much as possible, this background, and reveal details of how the GCR LET spectrum has varied over the complete solar activity cycle that has elapsed since LRO arrived at the Moon. In particular, previous work by Schwadron et al. (2014, 2018a), based in part on CRaTER measurements, predicted that GCR flux in the then-approaching solar minimum would exceed the historically high level that occurred in the previous solar minimum (Mewaldt et al., 2010), during which the LRO mission began. With that new minimum now upon us, we will test this prediction with these background-corrected measurements.

In the present work, we only consider the LET spectrum in the D5/6 detector pair for GCRs triggering all three thick detectors in the stack, which can be simply described as the spectrum under 9.9 g/cm^2 of shielding, mostly consisting of TEP. Case et al. (2013) considered, and the website provides, LET spectra for the D1/2 and D3/4 pairs for such triple-coincidence events as well, with the low-LET part of the spectrum measured by the thick detector of each pair and the high-LET part measured by the thin detector. The D1/2 and D3/4 spectra show differences due to different overlying shielding thicknesses as discussed by Zeitlin et al. (2013, 2016), but their variations are broadly similar to those of the D5/6 spectrum. The spectra in D1/2 or D3/4 also require additional caveats about the energy range of incident particles counted in each spectrum relative to what would be expected just from each detector pair's overlying shielding, since these spectra omit particles that would reach the D1/2 or D3/4 detector pairs and deposit energy there but that do not reach D5/6 to complete the coincidence. They merit further study with improved background rejection to follow up on the work of Zeitlin et al. (2013, 2016), but for the present work we focus on the more straightforward D5/6 LET spectrum.

1.2 Geant4 Simulations of CRaTER Response

In order to study the background response of CRaTER and how to reduce its contribution to the LET spectrum, we use the Geant4 radiation-transport code (Allison et al, 2006) to model the response of the sensor to cosmic rays arriving at it both inside and outside of the acceptance cone discussed above. Geant4 is an open-source toolkit that allows a user to model the transport of energetic particles of arbitrary species, location, and velocity through a three-dimensional material geometry, with or without electromagnetic fields. Stochastic processes like fluctuations of energy loss, nuclear interactions with target materials, and production of secondary particles are sampled from the appropriate probability distributions. Its primary use is to perform forward Monte Carlo simulations, whereby many energetic particles representing the radiation environment are launched into and then tracked through the geometry, with the code tabulating such quantities as energy deposit in detectors as particles' trajectories are modeled. Per the discussion in Section 1.1, we ensured accurate accounting of the effects of absorption and escape of secondary electrons by setting a "production cut" threshold of 10 μm, which is much smaller than the thin detectors. Geant4 assumes that all secondary electrons with ranges below this cut deposit their kinetic energy at the point of production, so that their contributions are collected in a continuous energy-loss process. However, any secondary electrons that would have longer

ranges are explicitly generated and tracked so that their possible escape from a detector, or arrival there after generation in adjacent inert matter, is accounted for with full physical realism.

Most of the CRaTER sensor head is exposed to space, with about a quarter of its sky filled by the body of the LRO spacecraft, and with no obstruction inside the D2/D6 acceptance cone (Spence et al., 2010). We use the simulations in Section 2.2 to inform the development of cuts to reject background events from the observations; we evaluate the effectiveness of those cuts, but in the present work we do not take the further step of subtracting the remaining estimated error from the observations, since that depends more sensitively on the modeled input GCR spectra over time. Thus we simulated the response of the sensor head floating in space, ignoring the modest reduction of the amplitude of the background signal that would occur due to the presence of the spacecraft. The simulated angular distribution incident on the sensor head is isotropic, omitting the portion of the sky blocked by the Moon at the 50 km nominal altitude of LRO (a cone with half-angle of 76° around the nadir).

The geometric model of the sensor head is the same as the one developed by Looper et al. (2013), and diagrammed therein. However, many improvements to the Geant4 code package have occurred since then, and in particular the version we used here (10.5, with Shielding_EMZ reference physics list) includes nuclear interactions of projectile ions heavier than helium with target materials (Allison et al., 2016), which were unavailable at the time of the work reported by Looper et al. (2013). We simulated incident ions from helium up to nickel (nuclear charge Z = 2 to 28) with energies from 10 MeV/nuc to 10 GeV/nuc; the upper limit was set by the available computer processing time, and omits about 3% of the total GCR flux. Simulations of proton projectiles run much faster than those of heavy ions, so we went to an upper energy of 100 GeV for hydrogen. We then weighted the simulation results with representative GCR spectra, as discussed below.

2 Background Rejection

2.1 Foreground and background signals

Figure 1 shows the simulated contributions to the dataset from GCR protons arriving either inside or outside the acceptance cone defined above. Each subpanel shows the distribution of the normalized energy deposits in the D4 and D6 detectors over all simulated events. The simulated sensor response is convolved with a GCR proton spectrum given by the Badhwar-O'Neill 2010 model (O'Neill, 2010) with modulation potential of 417 MV, which we found in previous work (Looper et al, 2013) to be a good representation for our purposes of the deep solar minimum at the start of the LRO mission (Mewaldt et al., 2010). The colorscale shows the logarithm of the countrate per 2-dimensional (D4 and D6) energy deposit bin in units of (sec $(keV/\mu m)^2)^{-1}$. The inset diagrams show a representation of the CRaTER stack of six detectors and two TEP cylinders, along with examples of trajectories of the kinds that contribute to each panel's population.

Figure 1a shows the set of particles whose LET we are trying to measure, i.e., those that reach the sensor head inside the acceptance cone. The track in the D4/D6 detector crossplot labeled "GCR protons" is caused by protons that simply penetrate the stack. In the energy range below about 1 GeV/nuc, the energy deposited by an ion per unit pathlength will decline with

increasing energy. Thus the right end of the track, at about 12 keV/μm in D6, is due to protons stopping in D6 or barely penetrating it, and depositing less energy in D4 since they traversed that detector before losing energy in the TEP cylinder between the D3/4 and D5/6 pairs. For incident protons of higher energy, the energy deposit in both D4 and D6 declines and their energy deposits populate the track to the left of its endpoint. As the proton energy gets high enough that the energy lost between D4 and D6 is a small fraction of its primary energy, the D4 and D6 energy deposits become more nearly equal and the track bends toward the diagonal (D4 = D6). Finally, relativistic protons reach a broad minimum in the curve of energy deposit vs. particle energy, and the particles' energy deposits cluster in the intense "minimum-ionizing particle" spot near the origin, at about 0.3 keV/μm in each detector.

The contribution to the LET spectrum in D6 of protons that deposit energy only via ionization is straightforward, and can easily be calculated from the primary GCR energy spectrum. However, protons that enter the sensor with sufficiently high energy may have nuclear interactions in the detectors or the TEP cylinders (the latter being more likely because of the greater column mass density of TEP) instead of just going straight through the stack. These protons can send fragments into D6 to deposit their energy, as sketched in the lower of the two trajectories in the inset of Figure 1a, with red "p+" label. These fragments are likely to include ions that have higher nuclear charge Z than the primary proton and that have lower energy per nucleon, both of which lead them to deposit more energy in D6. Thus we have the second labeled contribution to the crossplot in Figure 1a, with a small energy deposit in D4 from the high-energy primary proton and a large energy deposit in D5 and D6 due to the fragments. These must also be accounted for in the tabulation of the D5/6 LET spectrum, especially at higher energy deposits beyond the end of the direct proton track.

Figure 1b shows examples of the events that we are trying to exclude from our LET spectrum. A proton can miss one or more detectors, but still send out an energetic delta ray that travels to the missed detector(s) and completes the coincidence. Thus valid three- (or four-) detector coincidence events may be generated by ions that arrive outside the acceptance cone, even coming in through the side of the sensor head.

If the primary proton comes in fairly near the acceptance cone and misses D2 but a delta ray travels to D2 and triggers it, the proton's energy deposits in D4 and D6 may look very much like those of a proton arriving within the acceptance cone, as in the track labeled "Primaries missing D2." On the other hand, if a proton comes in at a steep angle and crosses only D5 and D6, but triggers D2 and D4 with a delta ray as in the example trajectory shown with red "p+" label, the energy deposit in D4 (and D2) will be a small amount due to the electron; however, the deposits in D5 and D6 can be large because of the long diagonal pathlength through them, even if the energy deposited per unit pathlength is small. These particles, labeled "Primaries missing D2/4," can look like the fragmentation events in Figure 1a. The challenge is to use the additional information in the D2 pulse height to develop cuts that can reject the events in Figure 1b while keeping the events in Figure 1a.

Figure 2 shows a similar crossplot of the simulated energy deposits in the thin detectors D1 and D5 due to all GCR ions up to nickel (Z = 1 to 28) coming from all directions, in or out of the acceptance cone. Here we also require that all six detectors are triggered for an event to be included in the plot, including all three thin detectors, to reduce background somewhat for illustrative purposes. The components of the track labeled "GCR protons" in Figure 1a are replicated for each element, but with energy deposits in each detector that are larger by a factor

of approximately Z^2. Like protons, iron ions produce a lower-energy track and a more intense spot due to relativistic ions, as labeled. There is a diagonal band below this due to the merged spots from lighter relativistic nuclei, and sub-relativistic tracks from the more abundant lighter elements (not labeled) extend horizontally off to the right for lower D1 energy deposits. There is an additional complication due to fragmentation of high-energy incident heavy nuclei in the detector/TEP stack, as discussed by Zeitlin et al. (2013) and also labeled in Figure 2. This is the inverse of the fragmentation process in Figure 1a, in that the lower-Z fragments of iron that reach D5/6 deposit less energy than the primary particle would have, not more. Most of the area of this plot comprises events that would saturate the thick detectors, so their energy deposits would be measured by D5 rather than (saturated) D6 in the LET spectra below. However, in the present work we do not require a coincidence of all six detectors as in this plot when measuring the high-LET part of the joint D5/6 spectrum, because in particular the sixfold coincidence would discard the contribution from high-Z fragments in Figure 1a (for which the delta ray would not trigger D1 or D3), and such events turn out to compose a significant fraction of the spectrum at higher LET.

2.2 Background rejection cuts

Because for events triggering all three thick detectors we have three measurements of energy deposits (counting D5 and D6 as a single measurement since, for events in the narrow energy-deposit range where both are triggered and neither is saturated, their signals will be nearly the same), we can attempt to devise sets of cuts that differentiate between foreground and background events that look indistinguishable using only two detectors' energy deposits, as in Figure 1. Figure 3 illustrates one such cut, showing crossplots of energy deposits in D2 and D5 for events that have a D4 energy deposit above 1.7 keV/μm (or a D5 deposit below 10 keV/μm, so the cut will not affect the dense population of events near the vertical axis). Ions arriving inside the acceptance cone and triggering D6 to complete the coincidence cannot be minimum-ionizing particles and deposit this much energy in D4, an amount well above that of an electron or relativistic proton. A relativistic proton coming into D2, and depositing a small amount of energy there, can only give a large energy deposit in D4 if a nuclear interaction occurs in the TEP between D1/2 and D3/4, but since the nuclear fragments would have short range they would not travel to D5/6 and complete the coincidence so as to be counted in this dataset. Figure 3a shows the simulated response to the subset of these GCRs arriving within the acceptance cone and having large D4 energy deposits. Indeed, among events with D5 energy deposits above 10 keV/μm there are very few events having low D2 energy deposits.

By contrast, a heavy ion can enter the side of the sensor head between D1/2 and D3/4, missing D2 but triggering it via a delta ray. Such an event would have large energy deposits in D4 and D5, but only a small deposit in D2 from the delta ray. Figure 3b shows the pattern of energy deposits in D2 and D5 for ions arriving outside the acceptance cone, and indeed we see many events with large D5 and small D2 energy deposits. Thus we may define by eye, based on the above physics logic, a cut shown by the white line in both Figures 3a and 3b, and reject events falling below it. As seen in Figure 3, this rejects many events due to particles arriving outside the acceptance cone, and few inside it. We evaluated many such subsets of the data, and devised a set of cuts that reject as many background events as possible while rejecting as few foreground events as possible. The cuts are spelled out as a logic statement in the Supporting Information, and we now apply them to the simulated and then the observed D5/6 LET spectra.

Figure 4 shows the contributions to D5/6 LET spectra due to different subsets of the simulated particle events, with Figure 4a calculated for the solar-minimum GCR spectrum used for the previous figures' simulations. Spectra below 20 keV/μm are calculated from D6 energy deposits, and above that from D5; different cuts are defined for each of these subsets, which is the reason for the discontinuities at this energy deposit in the two lowest curves (discussed below). The green "Raw" curve is the sum of all events due to ions arriving both in and out of the acceptance cone, and the red "Ideal" curve is the result only of those in the acceptance cone, which we are trying to attain with the cuts. The dark blue curve "With cuts" is the result of applying the cuts to the simulated particle events, and in most places it is significantly closer to the red curve than to the green curve.

The remaining differences are captured in the final two curves. "False positives" is the contribution from ions outside the acceptance cone that survive the cuts, and "False negatives" are due to ions inside it that are erroneously rejected. The fraction of false negatives is small at all energy deposits, and the contribution of false positives is significantly below the red curve at most places. However, at around 1 keV/μm and 10 keV/μm the contamination due to these false positives causes a noticeable difference between the blue result curve and the red ideal curve. This is due to the similarity between the patterns of energy deposit, in all three detectors, due to high-Z fragments as in Figure 1a and due to particles missing D2/4 as in Figure 1b. It is not possible to differentiate these two groups by the energy deposits of individual events, and we cannot reject all of the latter without rejecting at least some of the former as false negatives. Nonetheless significant background contribution to the signal is confined to the energy-deposit ranges around 1 keV/μm and 10 keV/μm and is less than 30% in these ranges, so these cuts are likely as good as can be devised.

Figure 4b shows the same contributions to the LET spectrum for GCR spectra under conditions of strong solar maximum modulation, in this case calculated from the Badhwar-O'Neill 2010 model with a modulation potential of 1000 MV. During solar maximum, GCR intensities are reduced relative to those at solar minimum, and lower energies are reduced more than higher. That is, the relativistic ions that produce the concentrated spots in Figures 1 and 2 are reduced less relative to Figure 4a than the lower-energy nuclei that produce the higher-energy-deposit tracks. Thus, when we produce a spectrum by summing over all energy deposits except those in D5/6, the peaks due to those hot spots stand out more from the smooth stretches in between them than is the case in Figure 4a.

As discussed above, the part of the background that is hardest to remove via cuts is mostly due to higher-energy ions, and so it is modulated less than the average of the ions producing the in-aperture signal. It therefore makes up a larger fractional background at solar maximum than at minimum, up to 45% of the "With cuts" spectrum at around 1 keV/μm and 10 keV/μm. Nonetheless, we have greatly reduced the background (difference between green "Raw" and blue "With cuts" curves), and we can apply the cuts to the observations with confidence that most of the variation that is seen in the background-rejected observations accurately reflects the changes in the underlying physical quantity that we are trying to measure.

3 Application of Cuts to the Observations

To extract GCR LET spectra from the CRaTER observations, we create a homogeneous dataset that omits periods of solar activity as seen in the countrates of single detectors (that is, with no solar particles even at energies well below those that can trigger multiple detectors as

analyzed herein), and that is restricted to times when LRO was in its nominal zenith-nadir orientation and at an altitude below 80 km. We then split the dataset into 6-month periods divided at day 66 and day 248 of each year through March 2020. The first period is slightly shorter, starting on day 259 of 2009, in order to match the time period analyzed by Looper et al. (2013) of deepest solar minimum at the start of the mission, between the start of the mission and the first Forbush decrease of the new solar cycle.

Figure 5 shows the raw LET spectrum derived from D5 and D6 as observed during this first time period (green curve), and the spectrum resulting from application of the cuts to reject background (red curve). The blue curve is the same as that in Figure 4a, created by applying the cuts to the simulated particle events drawn from the deep solar-minimum spectra for each GCR species. The differences between the blue and red curves, simulated and observed spectra with cuts, include not only any differences between the simulated and the actual instrument response, but also between the modeled and real input GCR spectra. Overall, though, the shapes, amplitude, and smoothness of these two curves match well, which gives us confidence that the cuts are having the expected effectiveness in rejecting background from the observed spectrum. We now examine the variations of these corrected observed spectra over the period from the past solar activity minimum to the present one.

4 Variation of GCR LET Spectra Over a Complete Solar Activity Cycle

As is implied by the simulated LET spectra in Figure 4, the variations over a solar activity cycle are subtle compared to the eight-decade dynamic range in a single spectrum across CRaTER's energy-deposit range. Figure 6 maps those variations onto a linear colorscale by dividing each time period's spectrum by the spectrum in the first period (which is therefore plotted as a constant 1.0). The peaks in the LET spectrum are due to higher-energy GCR ions than the spans between them, and thus the peaks are less affected by solar modulation than those spans. This is visible in Figure 6 in that the intensities at the locations of the peaks, labeled for several prominent GCR elements by their symbols at the right of the plot, decline only by about 30% at solar maximum in the middle of the plot, whereas the spans in between can decline by more than 60% at solar maximum.

The greatest decline with solar modulation is at an LET below 1 keV/μm, which lies between the peaks for relativistic H and He and is therefore due to sub-relativistic hydrogen. As seen in Figure 4, this is one of the places where the remaining "false positive" background is least effectively reduced. Since that background is due to relativistic protons and therefore modulated less than the causative particles whose effects we are trying to measure, the actual decline here will be slightly greater than measured. However, taking ratios between the raw LET spectra (with no background rejection) for the different time periods to produce a similar plot (not shown), we see a maximum decline of less than 50% at this location in the plot. Thus, the background rejection algorithm is making a significant improvement even here.

The colors of the band for the final time period in Figure 6 show that, as we travel through a new solar minimum as of this writing, the intensity of GCRs as seen in their LET spectra has returned to a level very near that measured during the historically-deep solar minimum at the start of the mission, as was recently reported using other CRaTER measurements by Zeitlin et al. (2019). Figure 7 plots the spectra from three time periods, the first and last at two solar minima and one from the solar maximum between them. The periods shown by each curve in Figure 7 are identified by bars of the same colors above the plot area in

Figure 6. To compress the eight-decade dynamic range in Figures 4 and 5 and make variations more apparent, the spectra are multiplied by the square of the normalized energy deposit against which they are plotted. Comparing the two solar-minimum periods, shown in red and blue, we see that over the LET range below about 10 keV/μm where the statistics are fairly good the latest period has in fact edged slightly above the intensity seen at the beginning of the mission. The difference so far is about 4%, though possibly less for heavier ions and higher LETs where statistics do not support identification of a difference. The green curve, in contrast, shows the greatest diminution of GCR intensity seen at solar maximum. The changing spectrum, accompanied by an indication of the corresponding period in a time series of sunspot number extracted from NASA/GSFC's OMNI dataset through OMNIWeb, is animated as a movie in the Supporting Information.

Figure 7 also includes a black curve indicating the standard deviation of the mean for the daily data sampled in each LET bin for the latest (blue) curve in the Figure. As the LRO orbit was changed throughout the mission, the fraction of each day meeting the criteria listed in Section 3 declined, reducing the number of particles included in each spectrum; thus this is the worst-case error among the data such that, e.g., the error for the red curve (not shown) would be a factor of four below this. The error as a fraction of the blue curve exceeds the 4% value quoted for its enhancement relative to the red curve over most of the LET range shown. However, this is the error calculated for each individual LET bin plotted (80 per decade), so a ratio taken over even a small LET range would encompass several bins and bring the combined error to a fraction of 4%; this is graphically shown in that the blue curve is visibly higher than the red curve below several keV/μm, even if the points for a few individual bins dip below it. Adding the statistical errors for each LET bin and time period in quadrature we observe that, in the LET range of 0.5 to 10 keV/μm, the flux of GCRs is on average 4.0% greater in the most recent six-month period than it was at the start of the mission, with a statistical uncertainty of 0.5%. Below this range, fluxes are dominated by relativistic protons that are not significantly enhanced in this solar minimum period relative to the one eleven years earlier, being higher by 0.35% with a statistical uncertainty of 0.30%. Above 10 keV/μm, the statistical uncertainty is large enough to obscure any increase that may be there, as seen in Figure 7. Integrating over the whole measured LET range to derive a dose rate (as described in the Appendix), we calculate a marginal increase from the past solar minimum to the current one of 1.4% with a statistical uncertainty of 0.9%.

Most possible sources of systematic instrumental error, such as the geometry factor calculated for the acceptance cone, would affect the LET spectra from all time periods the same way and so would not affect the comparison over time. As noted in Section 3, we restricted consideration to solar quiet times, during which the sensor's telemetry allocation allowed every particle event measured to be sent to the ground and during which deadtime was insignificant, so counting bias over time due to these factors is not an issue. One possible change over time would be due to detector gain drift, which would raise or lower the calculated spectra as channels narrowed or widened; however, the temperature-corrected gain that we used for these observations has been confirmed by an onboard pulser to be constant within 0.2% over the mission to date, so this is likewise not of concern. (We reduced the assumed gain in D5 by 8% to line its spectra up with those in D6 at LET values where they overlap, and with the locations of peaks in the simulations due to relativistic heavy elements, but this correction was applied to the whole dataset and again would have no effect on the comparison between time periods.) And while, as shown in Figure 5, the combination of the GCR model and Geant4 modeling of the

sensor response does not perfectly match the observations, any resulting errors in the cuts devised using that combination should have very nearly the same effects at the two solar minima in Figure 7, so that their effects would cancel out in the comparison between the red and blue curves. Thus we are confident in our estimate that, in the range of 0.5 to 10 keV/μm, the intensity of the GCR LET spectrum during the present solar minimum is 4% higher than in the solar minimum at the start of the mission.

5 Conclusions

5.1 Summary

CRaTER has now observed the interplanetary GCR from a vantage point aboard LRO in lunar orbit, outside the shielding provided by Earth's magnetosphere, over a complete 11-year solar activity cycle. To study the variations of the LET spectrum under 9.9 g/cm^2 of shielding in detectors D5 and D6 over this time, we used the energy deposits in individual detectors to devise cuts that separate particles arriving from space within the acceptance cone defined by detectors D2 and D6 from those arriving at the sensor head outside this acceptance cone. Unlike the background population that we seek to eliminate, the population of GCR ions entering the acceptance cone is well characterized in terms of their pathlengths through the detectors and the thickness of shielding through which they must pass. Thus, the resulting spectrum is straightforward to interpret and use in, e.g., studies of radiation shielding.

Applying our background-rejection algorithm to six-month periods spanning the LRO mission to date, we find that peaks in the spectrum that are due to relativistic GCR ions are modulated less than are the spans between them that are due to sub-relativistic ions; that the suppression of the intensity of parts of the LET spectrum that are most affected by the increased GCR modulation at solar maximum is measured at over 60%, and is probably slightly greater; and that as of early 2020, the intensity of GCRs has recovered and now slightly exceeds that during the historically-deep solar minimum at the start of the mission. Schwadron et al. (2014, 2018a) examined trends in the D1/2 dose rate (under much less shielding than the measurements analyzed here) to support a prediction based on solar activity and modulation patterns that the solar minimum that is now upon us would have even higher GCR intensities than the record-setting values recorded during the previous minimum. de Wet et al. (2020) and Rahmanifard et al. (2020) used the D5/6 dose rate (the same dataset as in this work, but with different cuts and normalization) to support a similar argument, with the latter paper including a period of measurements that matches ours and that also shows recovery of GCR intensity to a level at or slightly above that seen in the previous solar minimum. Breaking the difference between the two solar minima down by LET as in the present work, we find that the relativistic protons seen at LET below about 0.5 keV/μm are not much affected by any differences in modulation, while above about 10 keV/μm the statistics of our measurements in a six-month accumulation period do not allow any differences to be quantified with confidence. Between these two values of LET, however, we see evidence that solar modulation during the current solar minimum has weakened below the level seen in the past minimum, which is at least qualitatively consistent with the predictions of Schwadron et al. (2014, 2018a). We will continue to monitor and report these changes as the LRO mission continues, in order to provide quantitative limits on the depth of the modulation before it starts back up in the new solar cycle.

5.2 Future work

In this work we only considered the LET spectrum measured in detectors D5 and D6. Zeitlin et al. (2016) examined the variations with solar modulation of the LET spectra in D1 and D2, under much less shielding, for the same coincidence condition as used here (with D2, D4, and D6 required to have been triggered) but with a different algorithm for background rejection. As noted in Section 1, the spectra formed under this coincidence condition for D1/2 and D3/4 are not as straightforwardly described, since they omit energy deposit in D1/2 or D3/4 from particles that penetrate to each pair and deposit energy there but that do not travel to D5/6 to satisfy the coincidence requirement and be counted. However, this can be an advantage in that it enables us to examine the effects of fragmentation and secondary-particle production on the LET spectrum for the same population of particles in all three detector pairs, as was done by Zeitlin et al. (2016). We plan to revisit that analysis using the background-rejection algorithm developed here, or a further refinement. We will also look at the lower end of the LET spectra at least, where statistics are better, at finer time resolution, so as to look for effects of individual Forbush decreases as well as the overall solar-cycle variation reported here.

Also, in this work we used the combination of the Badhwar-O'Neill 2010 GCR model and Geant4 simulations of the sensor response to devise cuts that we applied to the CRaTER data to reject background events, but we only quantitatively compared observations to observations over time. We made no quantitative evaluation of the match between the observations and the predictions from the combination of GCR model and Geant4 simulations. We plan to perform such comparisons, with this and other subsets of the CRaTER data, and will use more recent GCR models for the comparisons.

It was remarked in Section 2.2 that, looking at the energy deposits of different individual particles, it was not possible to separate some valid populations from background populations, even with three detectors' measurements per particle event. However, the shape of the D4 energy-deposit spectrum that could be assembled for the particle events labeled "High-Z fragments" in Figure 1a will differ from the shape of that spectrum for those labeled "Primaries missing D2/4" in Figure 1b. By examining this, we may be able to exploit the different shapes to quantify and subtract the background contribution here in a statistical sense, rather than particle by particle as in the present work.

Finally, as noted in Section 1, CRaTER does not see many "albedo" secondary particles coming up from the Moon that have enough energy to penetrate the stack and trigger all three thick detectors, which means that the ones we do detect give at most two energy-deposit measurements, and thus we have less information to devise cuts to separate, e.g., the albedo proton track from its background. We have devised a method akin to the statistical procedure outlined above to perform background subtraction for these observations (Schwadron et al., 2018b), and we plan to improve that algorithm and apply it to our measurements of lunar albedo protons.

Acknowledgments and Data

This work was funded by the NASA LRO program (contract NNG11PA03C). The Level-2 CRaTER data products and attitude/ephemeris information used in this paper are available online (http://crater-web.sr.unh.edu), and the full data set is archived at the Planetary Plasma Interactions (PPI) Node of the Planetary Data System (PDS; https://pds-ppi.igpp.ucla.edu). We

acknowledge use (in the Supporting Information) of NASA/GSFC's Space Physics Data Facility's OMNIWeb service, and OMNI data.

Appendix A: Calculation of Dose Rates from LET Spectra

An LET spectrum allows evaluation of the differing effects of particles that deposit different amounts of energy in a sensitive target; by contrast, specifying total radiation dose or dose rate aggregates different particle populations' effects into a single number. However, a single number is simpler to deal with when tracking time variations, for example, and so we show here how to calculate a dose rate from an LET spectrum.

Consider a sensitive target of arbitrary shape, represented in Figure A1 by the blue sphere. For a given direction, the particle flux j can be represented per unit LET (and time, area, and solid angle), i.e, in units as on the ordinate of Figures 4 and 5, instead of per unit primary-particle energy as is usual. Then the rate of particles per unit LET reaching the target from the given direction within a small solid angle $d\Omega$ and into a small area dA normal to that direction is $jdAd\Omega$. Let the length of the portion of a particle's trajectory through the target from that direction and into area dA be L, and let the particle's LET (actually the similar lineal energy, or energy deposited per unit pathlength, as discussed in Section 1) be λ, so that $j = j(\lambda)$; then the rate of energy deposit into the target for those particles (still per unit LET) will be $\lambda LjdAd\Omega$.

Integrating over dA to cover the whole target from this direction, the rate of energy deposit in the target per unit LET will be $\lambda jd\Omega \int LdA$. But $\int LdA$ is just the volume V of the target; if the target has density ρ and therefore mass $M = \rho V$, then the rate of energy deposit per unit LET in this small solid angle $d\Omega$ will be $\lambda jMd\Omega/\rho$. And, since dose is energy deposit per unit mass, the dose rate per unit LET from this direction will be $\lambda jd\Omega/\rho$. (It is common to specify LET not per unit length in a specific material, which we have called λ, but per unit column mass density, which we can call $\Lambda = \lambda/\rho$, for easier comparison of different target materials. In terms of this latter quantity, the dose rate per unit LET from a single direction will be just $\Lambda jd\Omega$.)

This can be convolved with the LET spectra from different directions, if they are altered by different thicknesses of shielding; assuming isotropic shielding and therefore j, we simply integrate over all directions to get a dose rate per unit LET of $4\pi\lambda j/\rho$. Integrating this over $d\lambda$ for the spectra measured at the time periods in Figure 6, we obtain the dose rate variation under 9.9 g/cm^2 of shielding as shown in Figure A2.

These values are measured in orbit around the Moon, with almost half the sky blocked by its disk, but since they are directional measurements looking zenithward that are then integrated over 4π sr they are effectively measurements of the unobstructed interplanetary dose rate, about 13.9 rads (or 13.9 cGy) per year at the start of the mission. For comparison, Mazur et al. (2011) reported a dose rate of 19 rads per year in a microdosimeter housed within the CRaTER electronics box during translunar cruise at the start of the LRO mission. This was an omnidirectional measurement, meaning that a large fraction of the sky was shielded by the body of the spacecraft, while in the direction outward from the microdosimeter location the shielding was about 4.4 g/cm^2 (Mazur et al., 2015).

Schwadron et al. (2014) used the energy deposits in D1/2 to calculate a dose rate of about 13.5 rads per year in lunar orbit at the start of the mission. This was also an omnidirectional measurement, with only 0.3 g/cm^2 of shielding in front of D1 but with the Moon covering almost

half the sky in the opposite direction, so that we might estimate the free-space dose at something like twice this or 27 rads per year. Due to these differences of geometry, the three measurements are not directly comparable. Nonetheless, they give an idea of the range of dose rate under different shielding due to GCRs during solar minimum, a range that is not very large because most of the particles contributing to this dose are very penetrating and not much diminished by shielding in the range considered (0.3 to 9.9 g/cm^2).

References

Allison et al. (2006), Geant4 Developments and Applications. *IEEE Transactions on Nuclear Science*, *53*(1), 270-278. doi:10.1109/TNS.2006.869826

Allison et al. (2016), Recent Developments in Geant4. *Nuclear Instruments and Methods in Physics Research A*, *835*, 186-225. doi:10.1016/j.nima.2016.06.125

Case, A. W., Kasper, J. C., Spence, H. E., Zeitlin, C. J., Looper, M. D., Golightly, M. J., Schwadron, N. A., Townsend, L. W., Mazur, J. E., Blake, J. B., and Iwata, Y. (2013), The Deep-Space Galactic Cosmic Ray Lineal Energy Spectrum at Solar Minimum. *Space Weather*, *11*(6), 361-368. doi:10.1002/swe.20051

de Wet, W. C., Slaba, T. C., Rahmanifard, F., Wilson, J. K., Jordan, A. P., Townsend, L. W., Schwadron, N. A., and Spence, H. E. (2020), CRaTER Observations and Permissible Mission Duration for Human Operations in Deep Space. *Life Sciences in Space Research*, *26*, 149-162. doi:10.1016/j.lssr.2020.04.004

International Commission on Radiological Protection (1991), Annex A: Quantities Used in Radiological Protection. *Annals of the ICRP*, *21*(1-3), 79-89. doi:10.1016/0146-6453(91)90073-P

Looper, M. D., Mazur, J. E., Blake, J. B., Spence, H. E., Schwadron, N. A., Golightly, M. J., Case, A. W., Kasper, J. C., and Townsend, L. W. (2013), The Radiation Environment Near the Lunar Surface: CRaTER Observations and Geant4 Simulations. *Space Weath*er, *11*(4), 142-152. doi:10.1002/swe.20034

Mazur, J. E., Crain, W. R., Looper, M. D., Mabry, D. J., Blake, J. B., Case, A. W., Golightly, M. J., Kasper, J. C., and Spence, H. E. (2011), New Measurements of Total Ionizing Dose in the Lunar Environment. *Space Weather*, *9*(7), S07002. doi:10.1029/2010SW000641

Mazur, J. E., Zeitlin, C., Schwadron, N., Looper, M. D., Townsend, L. W., Blake, J. B., and Spence, H. (2015), Update on Radiation Dose from Galactic and Solar Protons at the Moon Using the LRO/CRaTER Microdosimeter. *Space Weather*, *13*(6), 363-364. doi:10.1002/2015SW001175

Mewaldt, R. A., Davis, A. J., Lave, K. A., Leske, R. A., Stone, E. C., Wiedenbeck, M. E., Binns, W. R., Christian, E. R., Cummings, A. C., de Nolfo, G. A., Israel, M. H., Labrador, A. W., and von Rosenvinge, T. T. (2010), Record-Setting Cosmic-Ray Intensities in 2009 and 2010. *Astrophysical Journal Letters*, *723*, L1. doi:10.1088/2041-8205/723/1/L1

O'Neill, P. M. (2010), Badhwar-O'Neill 2010 Galactic Cosmic Ray Flux Model – Revised. *IEEE Transactions on Nuclear Science*, *57*(6), 3148-3153. doi:10.1109/TNS.2010.2083688

Rahmanifard, F., de Wet, W. C., Schwadron, N. A., Owens, M. J., Jordan, A. P., Wilson, J. K., Joyce, C. J., Spence, H. E., Smith, C. W., and Townsend, L. W. (2020), Galactic Cosmic Radiation in the Interplanetary Space Through a Modern Secular Minimum. *Space Weather*, *18*(9), e2019SW002428. doi:10.1029/2019SW002428

Schwadron, N. A., Blake, J. B., Case, A. W., Joyce, C. J., Kasper, J., Mazur, J., Petro, N., Quinn, M., Porter, J. A., Smith, C. W., Smith, S., Spence, H. E., Townsend, L. W., Turner, R., Wilson, J. K., and Zeitlin, C. (2014), Does the Worsening Galactic Cosmic Radiation Environment Observed by CRaTER Preclude Future Manned Deep Space Exploration? *Space Weather*, *12*(11), 622-632. doi:10.1002/2014SW001084

Schwadron, N. A., Rahmanifard, F., Wilson, J., Jordan, A. P., Spence, H. E., Case, A. W., de Wet, W., Farrell, W. M., Kasper, J. C., Looper, M. D., Lugaz, N., Mays, L., Mazur, J. E., Niehof, J., Petro, N., Smith, C. W., Townsend, L. W., Winslow, R., and Zeitlin, C. (2018a), Update on the Worsening Particle Radiation Environment Observed by CRaTER and Implications for Future Human Deep-Space Exploration. *Space Weather*, *16*(3), 289-303. doi:10.1002/2017SW001803

Schwadron, N. A., Wilson, J. K., Jordan, A. P., Looper, M. D., Zeitlin, C., Townsend, L. W., Spence, H. E., Legere, J., Bloser, P., Farrell, W. M., Hurley, D., Petro, N., Stubbs, T. J., and Pieters, C. (2018b), Using Proton Radiation from the Moon to Search for Diurnal Variation of Regolith Hydrogenation. *Planetary and Space Science*, *162*, 113-132. doi:10.1016/j.pss.2017.09.012

Smathers, J. B., Otte, V. A., Smith, A. R., Almond, P. R., Attix, F. H., Spokas, J. J., Quam, W. M., and Goodman, L. J. (1977), Composition of A-150 Tissue-Equivalent Plastic. *Medical Physics*, *4*(1), 74-77. doi:10.1118/1.594380

Spence, H. E., Case, A. W., Golightly, M. J., Heine, T., Larsen, B. A., Blake, J. B., Caranza, P., Crain, W. R., George, J., Lalic, M., Lin, A., Looper, M. D., Mazur, J. E., Salvaggio, D., Kasper, J. C., Stubbs, T. J., Doucette, M., Ford, P., Foster, R., Goeke, R., Gordon, D., Klatt, B., O'Connor, J., Smith, M., Onsager, T., Zeitlin, C., Townsend, L. W., & Charara, Y. (2010), CRaTER: The Cosmic Ray Telescope for the Effects of Radiation Experiment on the Lunar Reconnaissance Orbiter Mission. *Space Science Reviews*, *150*, 243-284. doi:10.1007/s11214-009-9584-8

Wilson, J. K., Spence, H. E., Schwadron, N. A., Case, A. W., Looper, M. D., Jordan, A. P., de Wet, W., and Kasper, J. C. (2019), Precise Detections of Solar Particle Events and a New View of the Moon. *Geophysical Research Letters*, *47*(1), e2019GL085522. doi:10.1029/2019GL085522

Zeitlin, C., Case, A. W., Spence, H. E., Schwadron, N. A., Golightly, M., Wilson, J. K., Kasper, J. C., Blake, J. B., Looper, M. D., Mazur, J. E., Townsend, L. W., and Iwata, Y. (2013), Measurements of Galactic Cosmic Ray Shielding with the CRaTER Instrument. *Space Weather*, *11*(5), 284-296. doi:10.1002/swe.20043

Zeitlin, C., Case, A. W., Schwadron, N. A., Spence, H. E., Mazur, J. E., Joyce, C. J., Looper, M. D., Jordan, A., Rios, R. R., Townsend, L. W., Kasper, J. C., Blake, J. B., Smith, S., Wilson, J., and Iwata, Y. (2016), Solar Modulation of the Deep Space Galactic Cosmic Ray Lineal Energy Spectrum Measured by CRaTER, 2009-2014. *Space Weather*, *14*(3), 247-258. doi:10.1002/2015SW001314

Zeitlin, C., Schwadron, N. A., Spence, H. E., Jordan, A. P., Looper, M. D., Wilson, J., Mazur, J. E., and Townsend, L. W. (2019). Update on Galactic Cosmic Ray Integral Flux Measurements in Lunar Orbit with CRaTER. *Space Weather*, *17*(7), 1011-1017. doi:10.1029/2019SW002223

Figure Captions

Figure 1: Crossplots of simulated energy deposits in D4 and D6 detectors from GCR protons. Inset diagrams show examples of particle trajectories contributing to each plot. (a) Foreground signal from protons arriving within the acceptance cone, showing events contributing to the LET spectrum in D5 and D6. (b) Background signal from protons arriving from all other directions except those blocked by the Moon, showing events that may be confused with the foreground signal.

Figure 2: Crossplot of simulated energy deposits in D1 and D5 detectors from all GCR ions up to nickel, both inside and outside the acceptance cone. Portions of the event population due to GCR iron are labeled.

Figure 3: Crossplot of simulated energy deposits in D2 and D5 detectors for all GCR ions up to nickel having energy deposits in D4 above 1.7 keV/μm, with a white line indicating the cut described in the main text. (a) Events due to particles arriving within the acceptance cone, showing few events below the cut line. (b) Events due to particles arriving from outside the acceptance cone, showing many events below the line that can be rejected by the cut.

Figure 4: Effectiveness of cuts on simulated D5/6 LET spectra. (a) Solar minimum GCR spectra. (b) Solar maximum GCR spectra.

Figure 5: Effect of cuts on observed D5/6 LET spectrum compared with simulations.

Figure 6: Ratios between measured LET spectra for each 6-month period and the spectrum from the first period (shown as solid red, or unity on the linear colorscale). Energy deposit values where peaks due to relativistic ions are less modulated are labeled with the applicable element's symbol at right. Red, green, and blue bars above the plot identify time periods plotted in Figure 7.

Figure 7: LET spectra at two solar minima and the solar maximum between them, from the periods identified by bars of the same colors as these curves above the plot in Figure 6. Black curve shows the standard deviation of the mean of the daily measurements for the individual LET bins composing the blue curve. All curves are multiplied by the square of the abscissa, to compress the dynamic range.

Figure A1: Geometry for calculation of dose rate from LET spectrum.

Figure A2: Dose rates calculated from the LET spectra for the six-month periods in Figure 6, integrated over all look directions in an unobstructed 4π sr.

Figure 1.

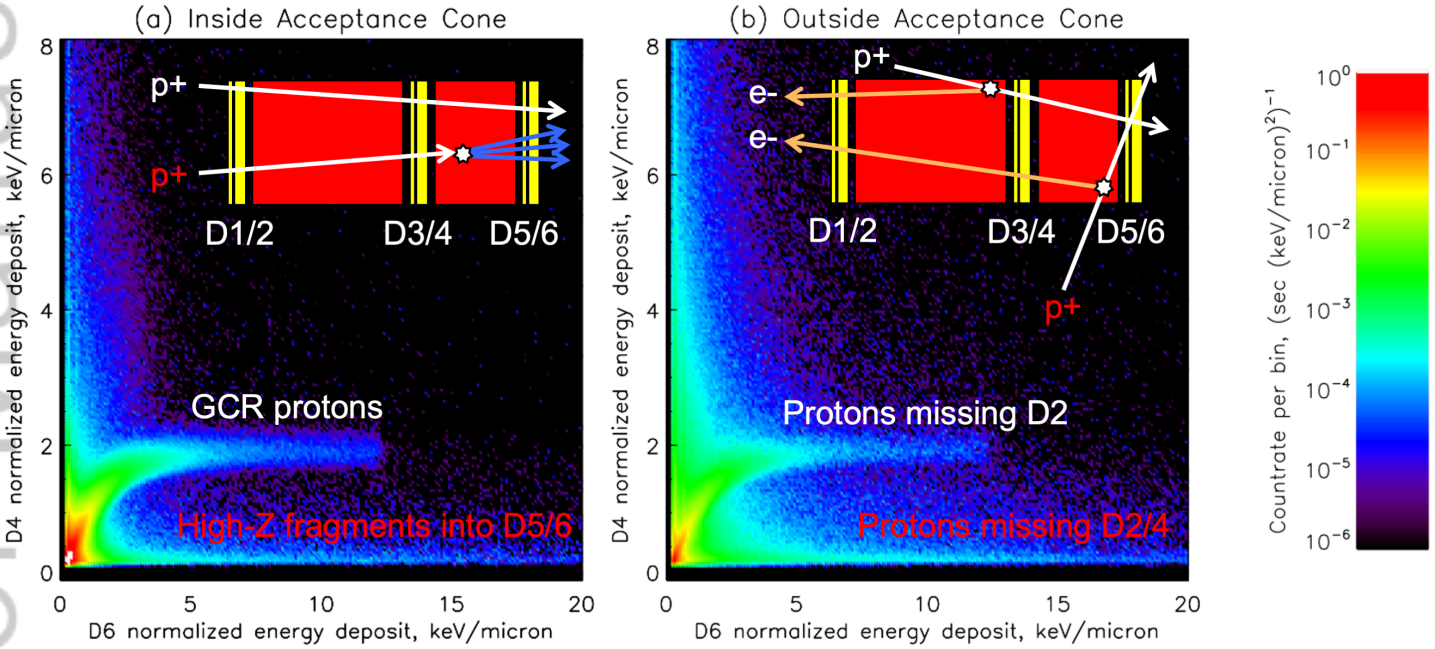

Figure 2.

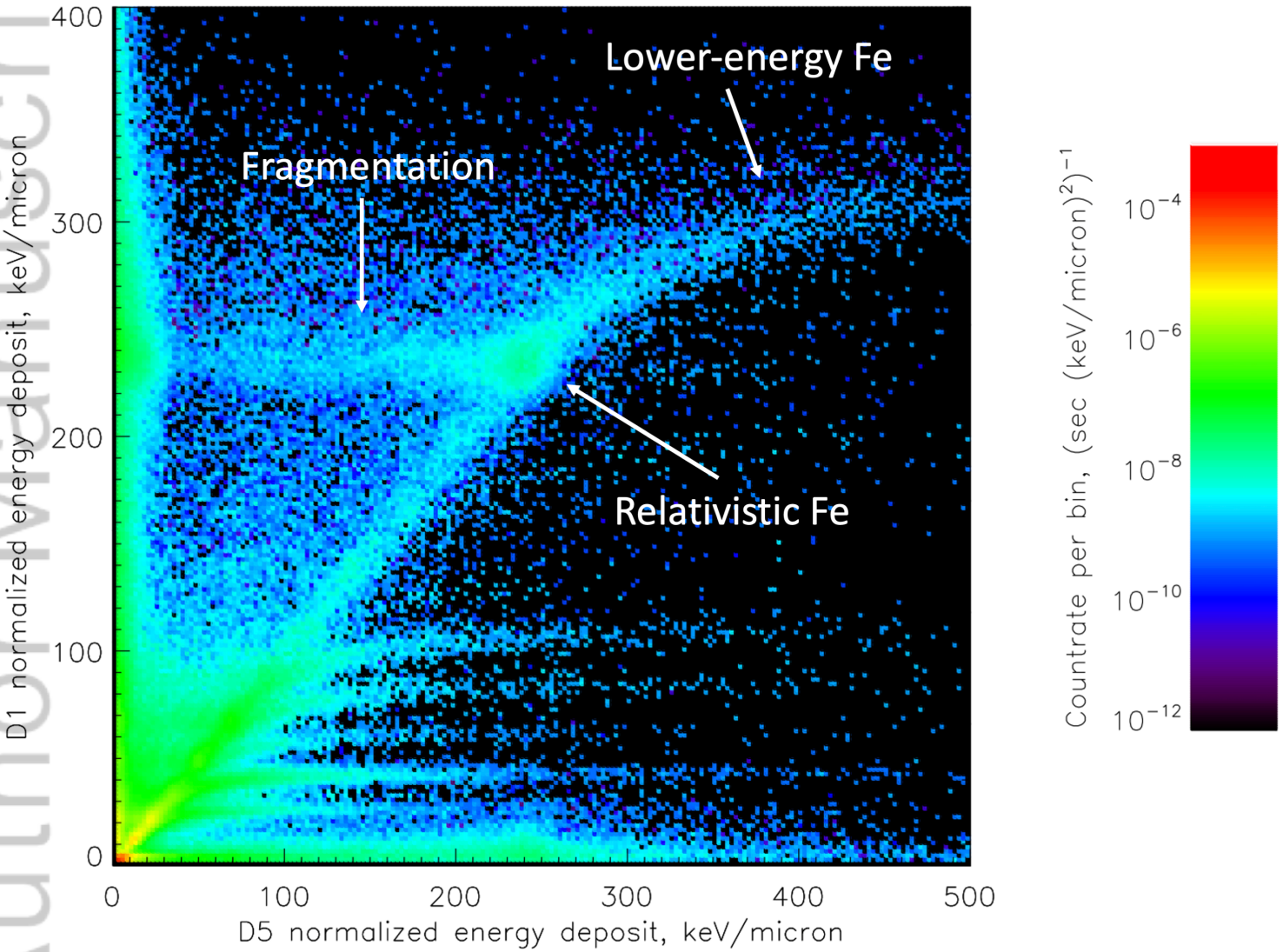

Figure 3.

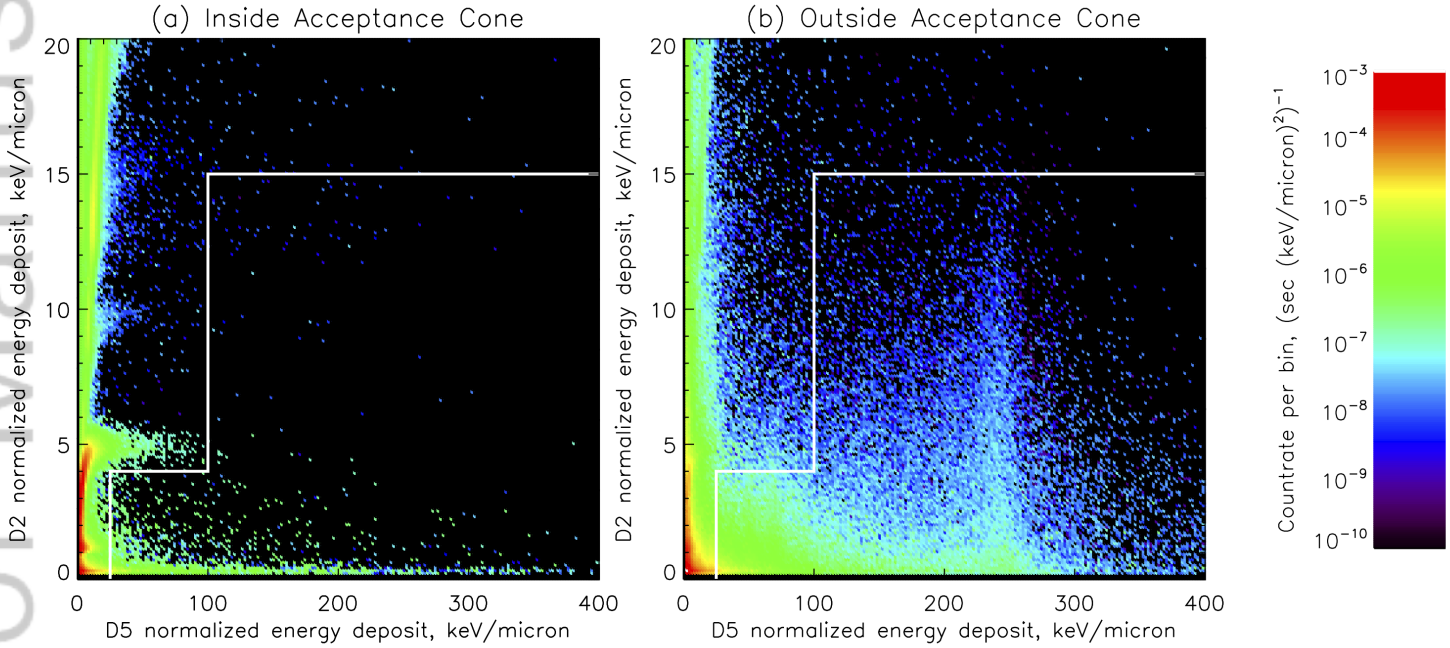

Figure 4.

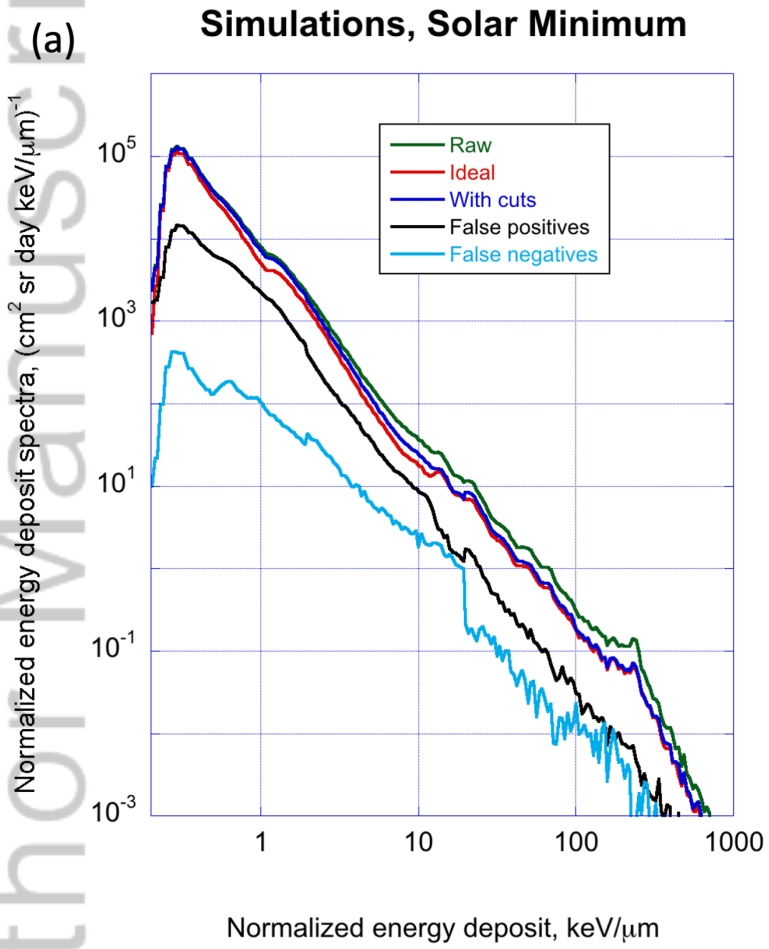

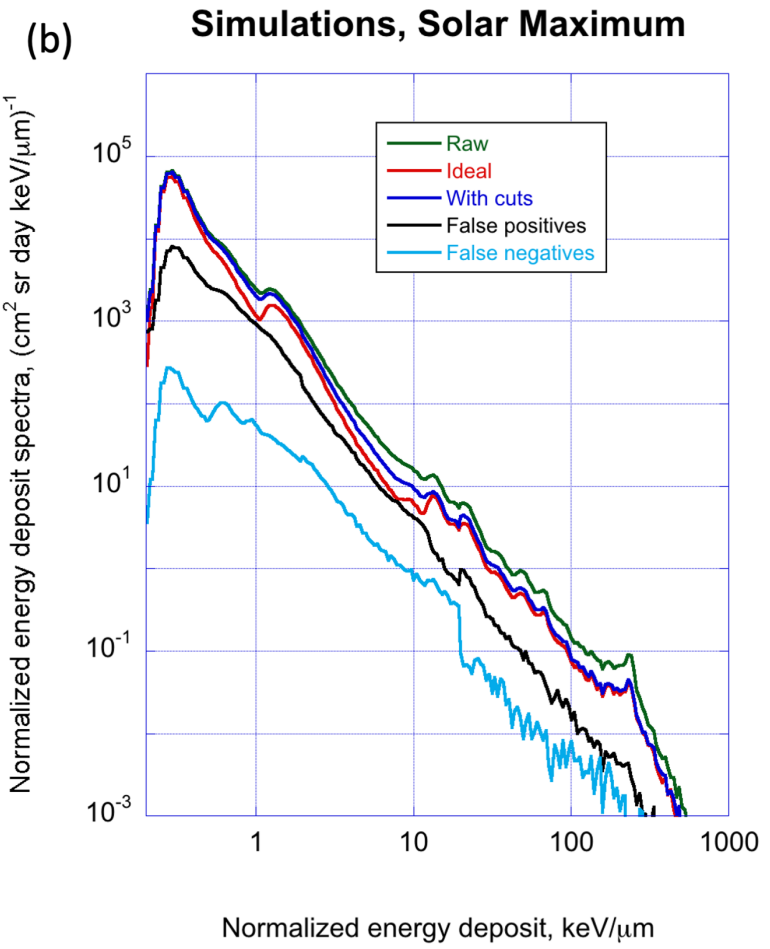

Figure 5.

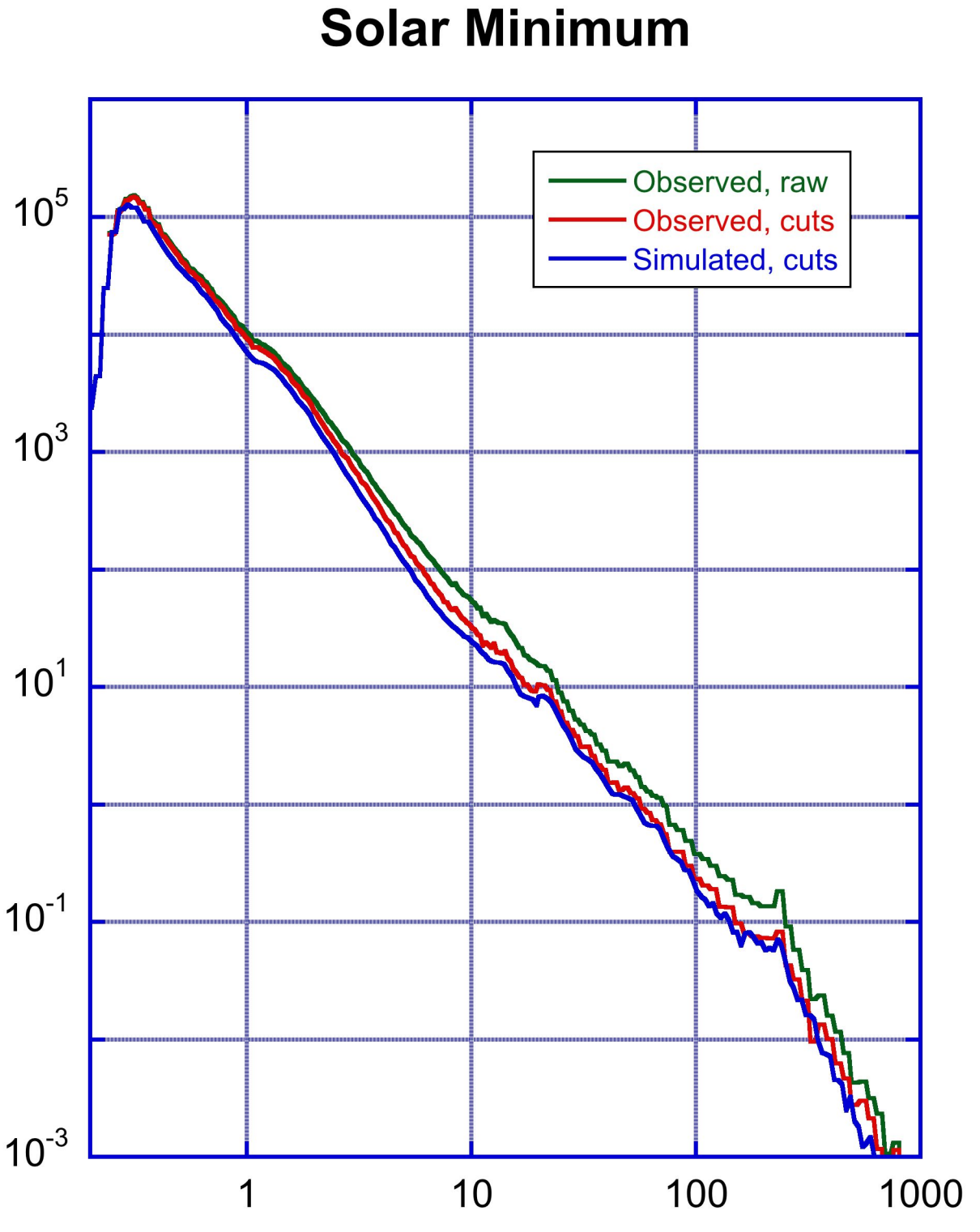

Figure 6.

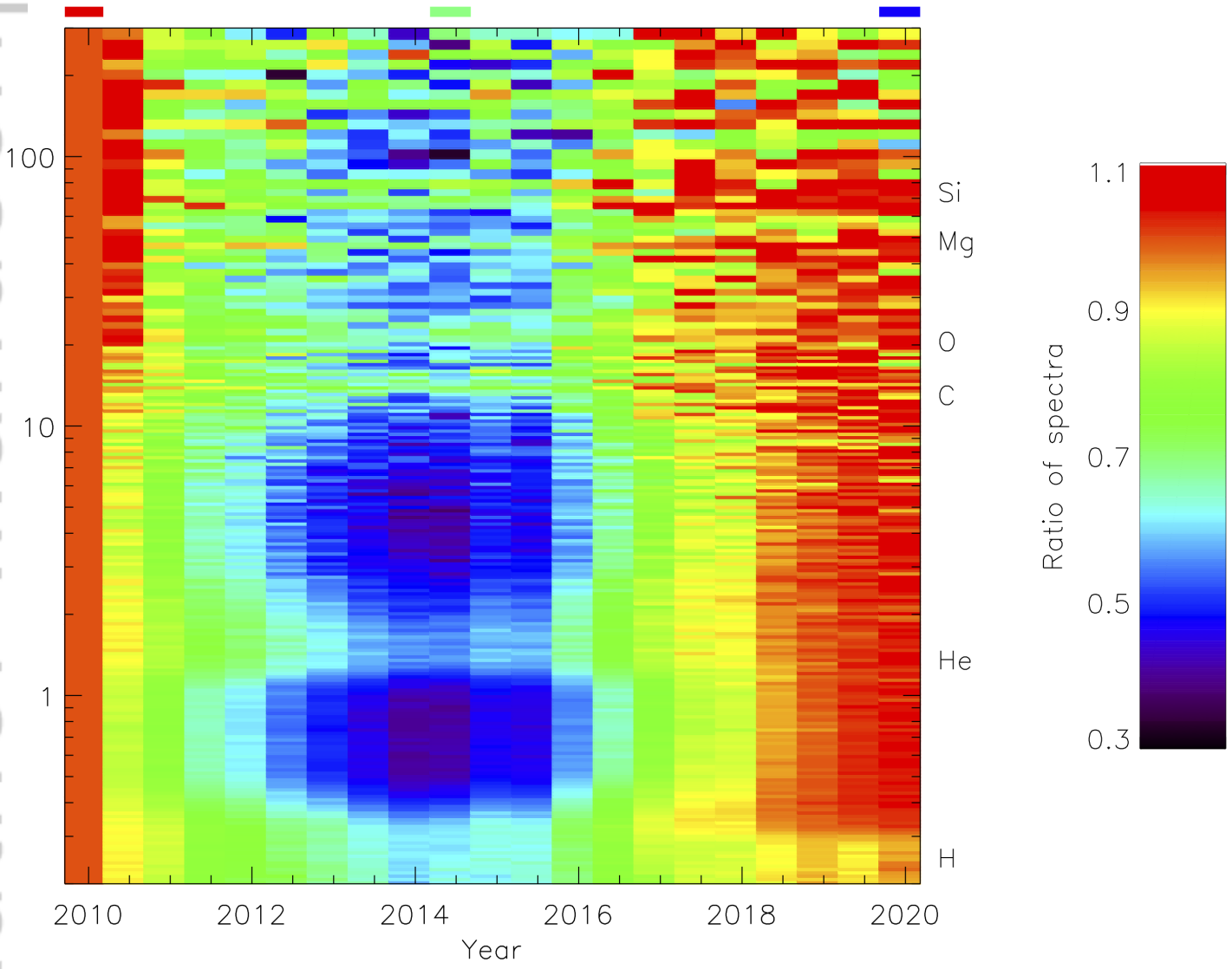

Figure 7.

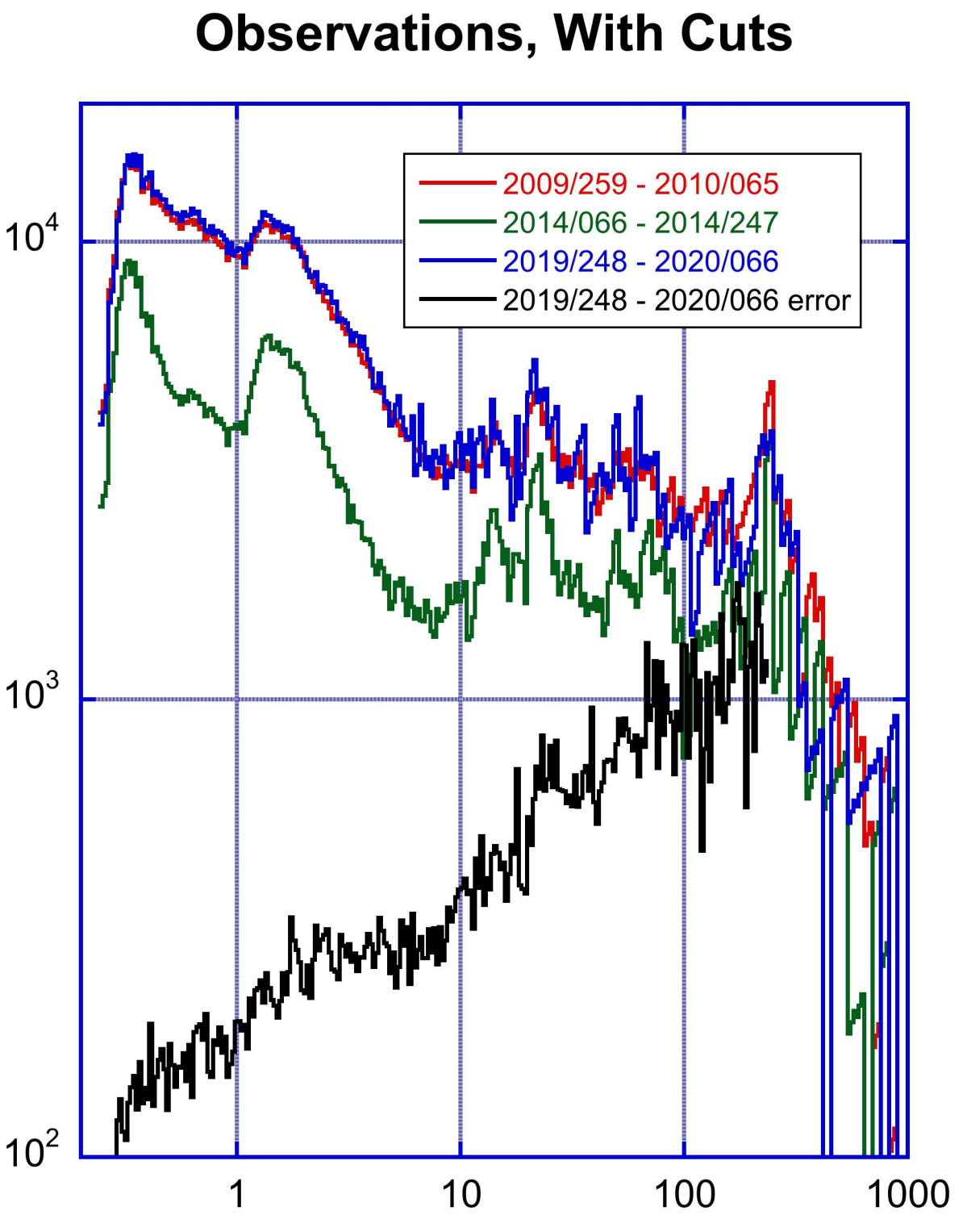

Figure A1.

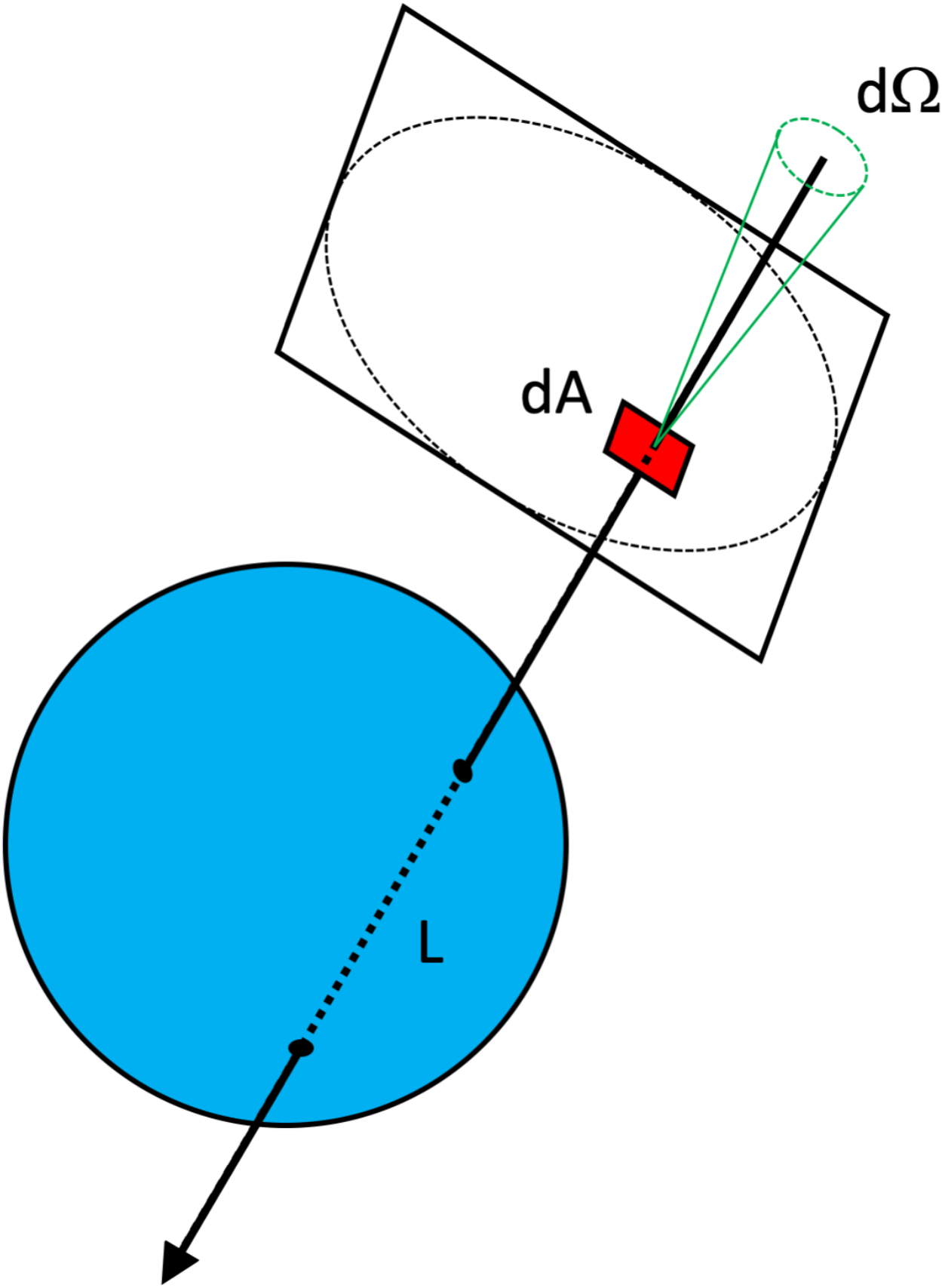

Figure A2.

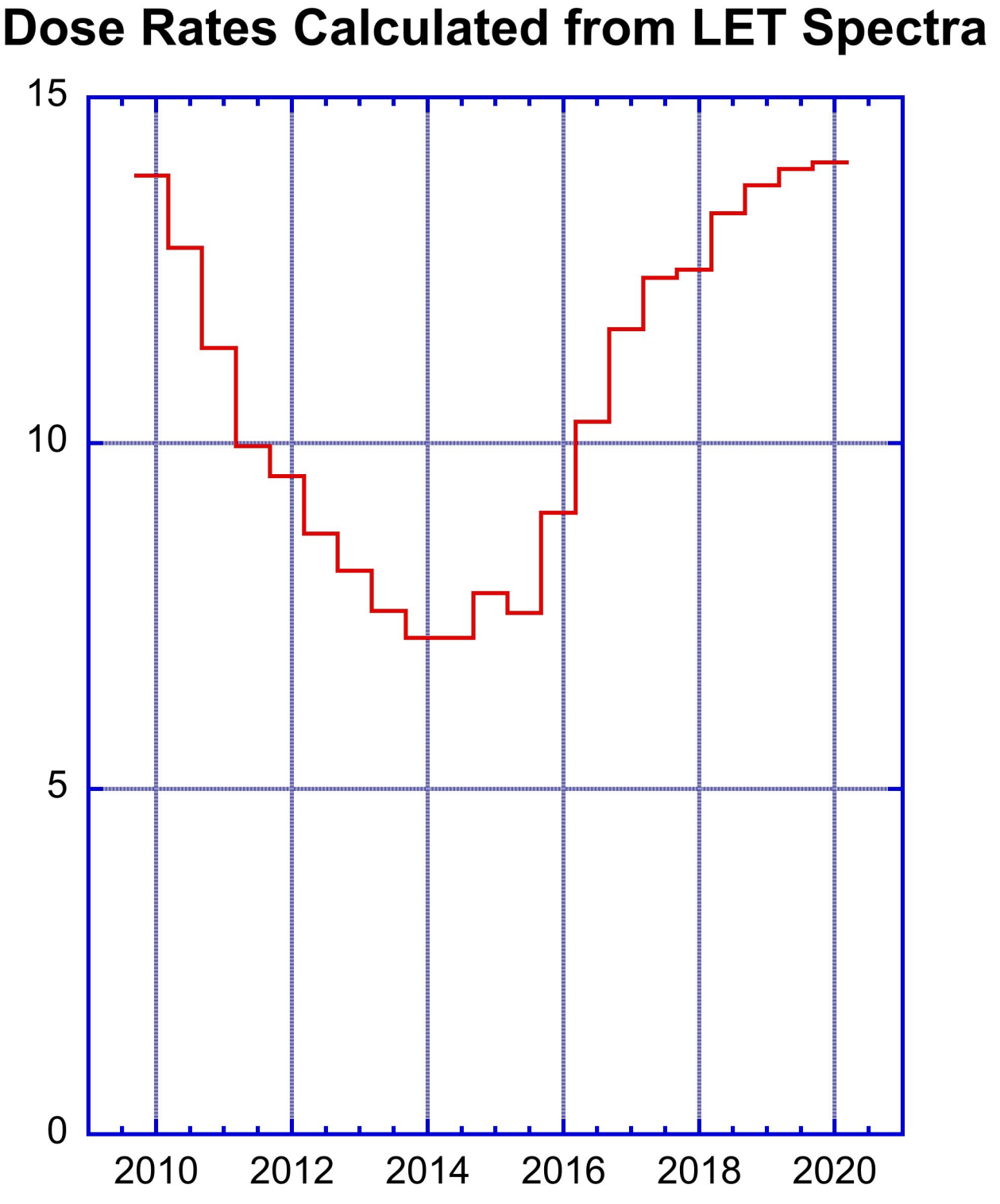

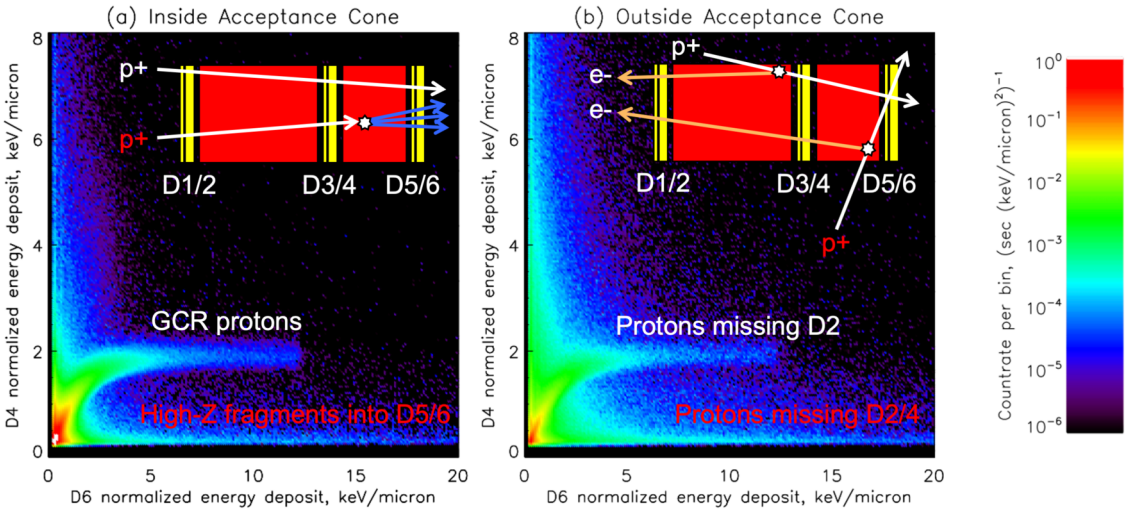

SWE_21079_2020SW002543-f01-z-.tif

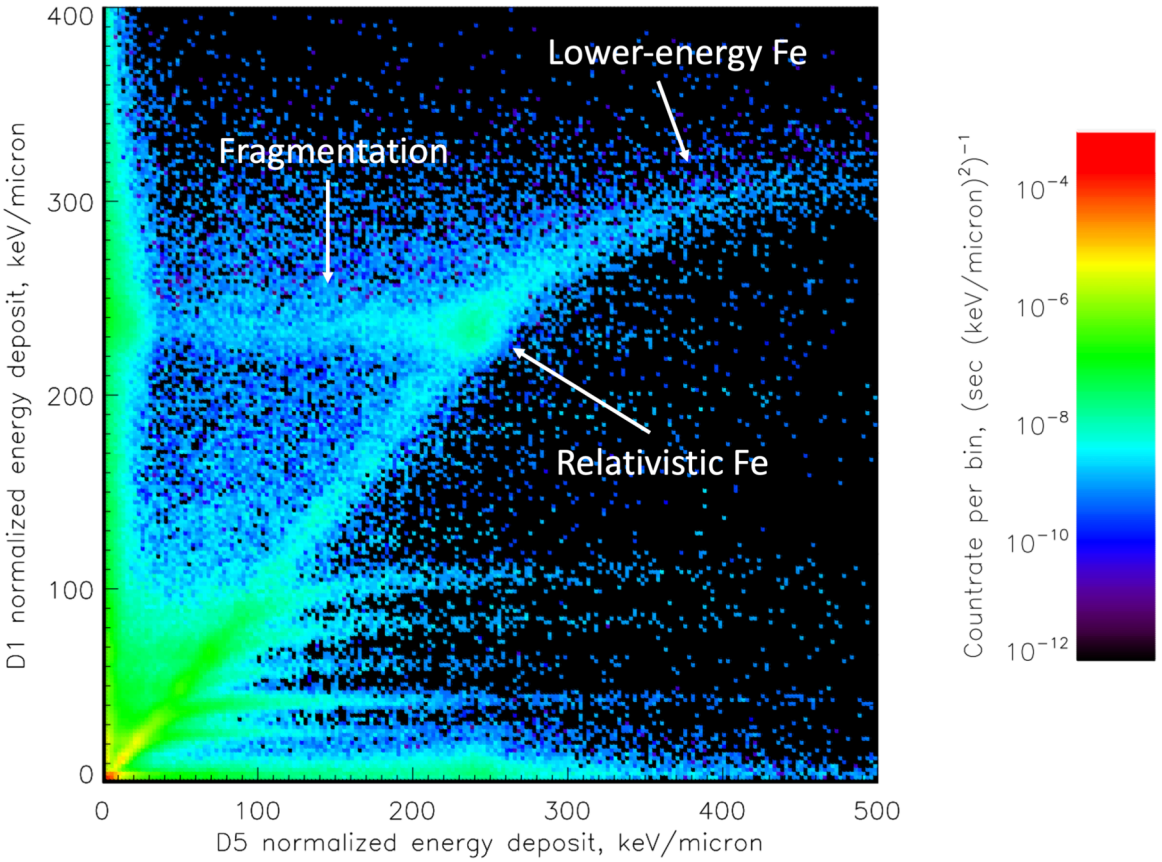

SWE_21079_2020SW002543-f02-z-.tif

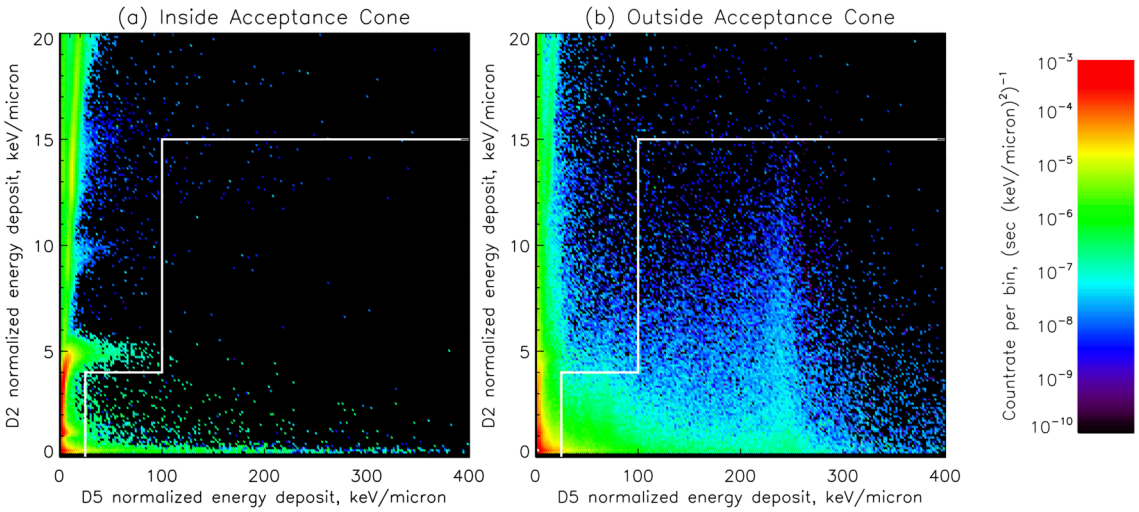

SWE_21079_2020SW002543-f03-z-.tif

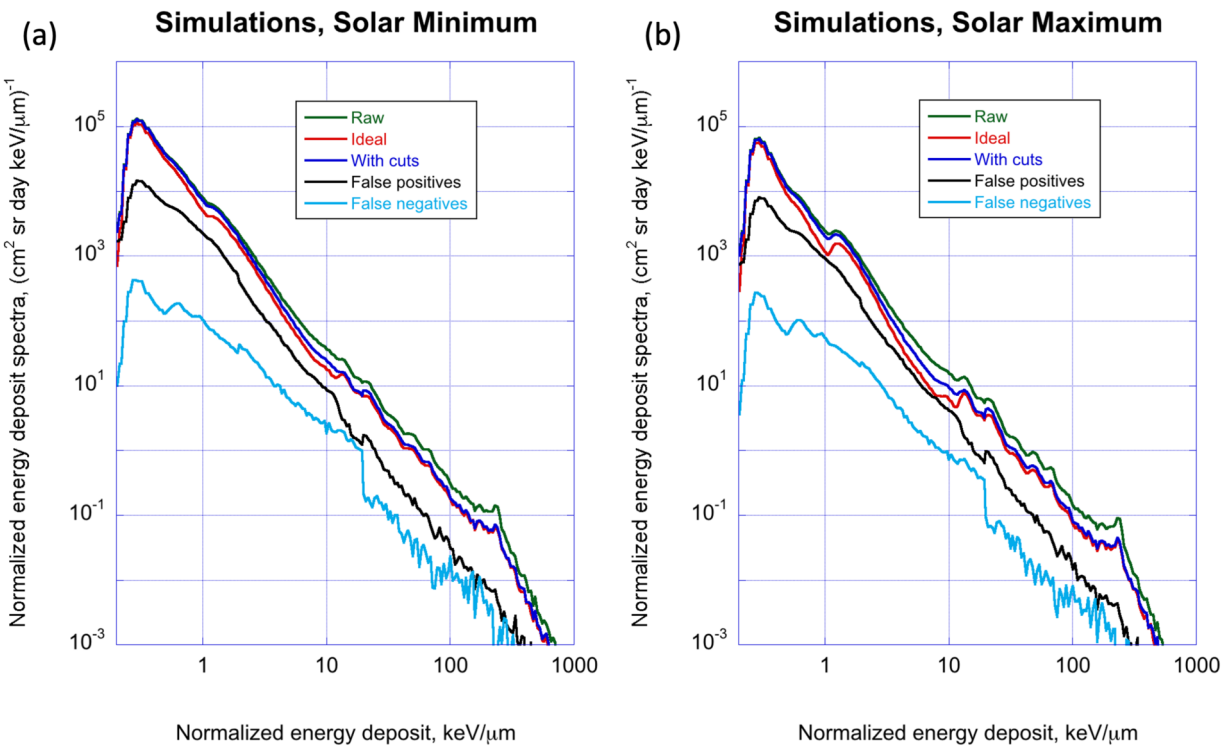

SWE_21079_2020SW002543-f04-z-.tif

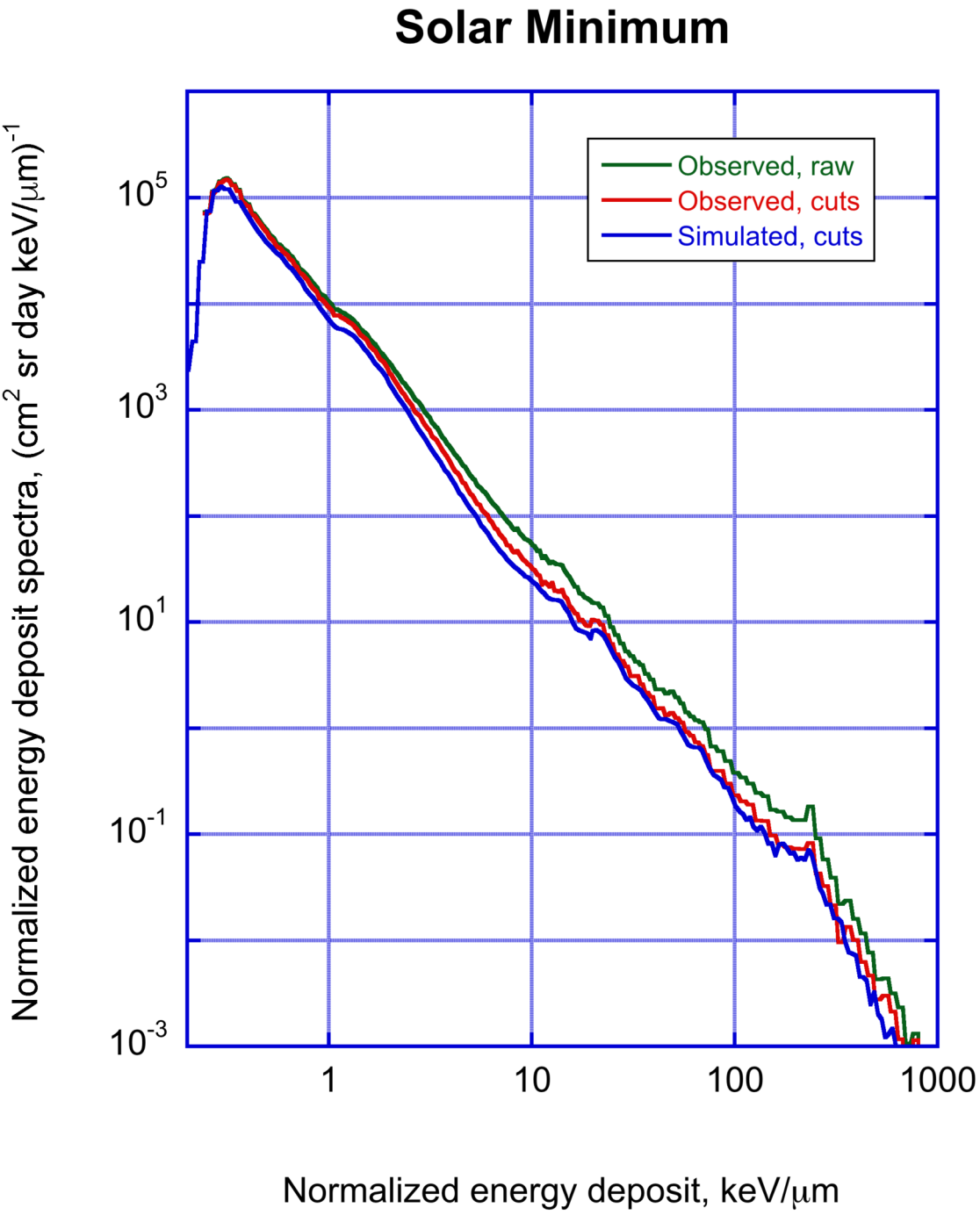

SWE_21079_2020SW002543-f05-z-.tif

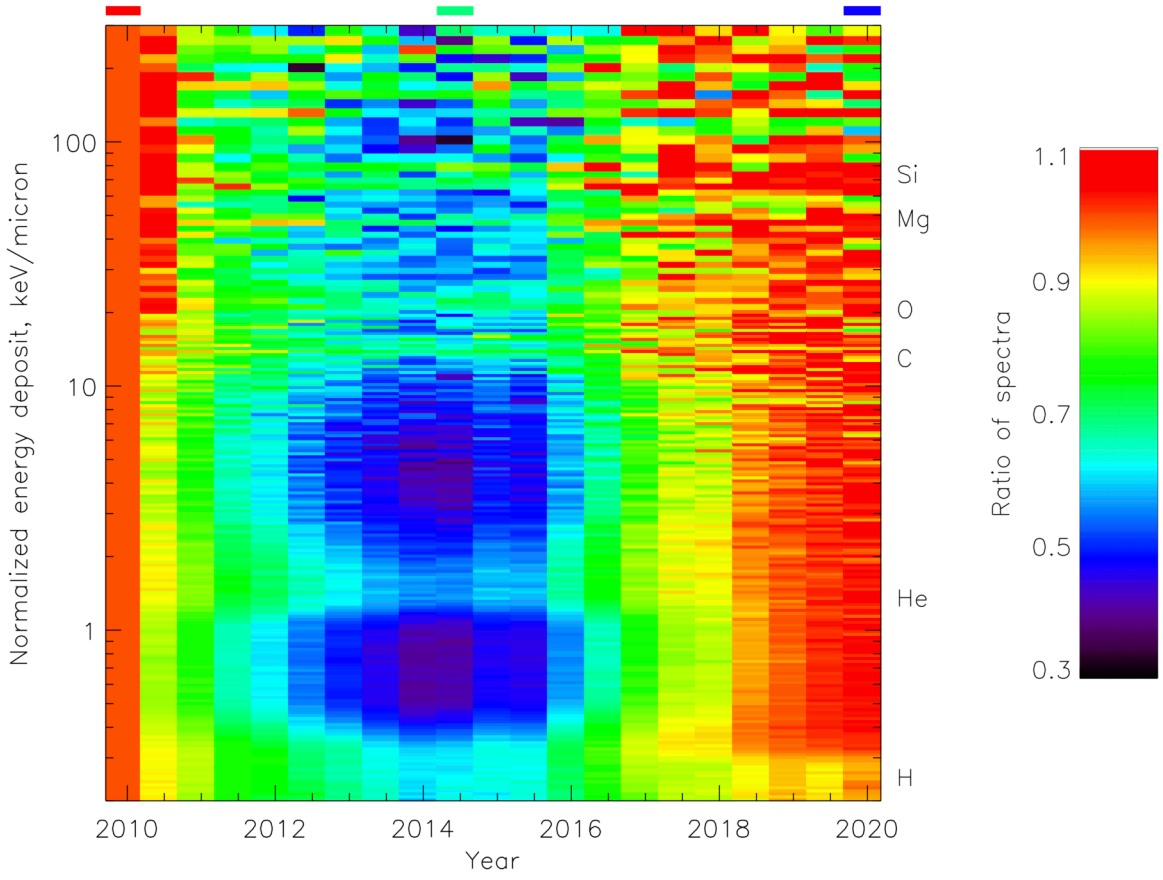

SWE_21079_2020SW002543-f06-z-.tif

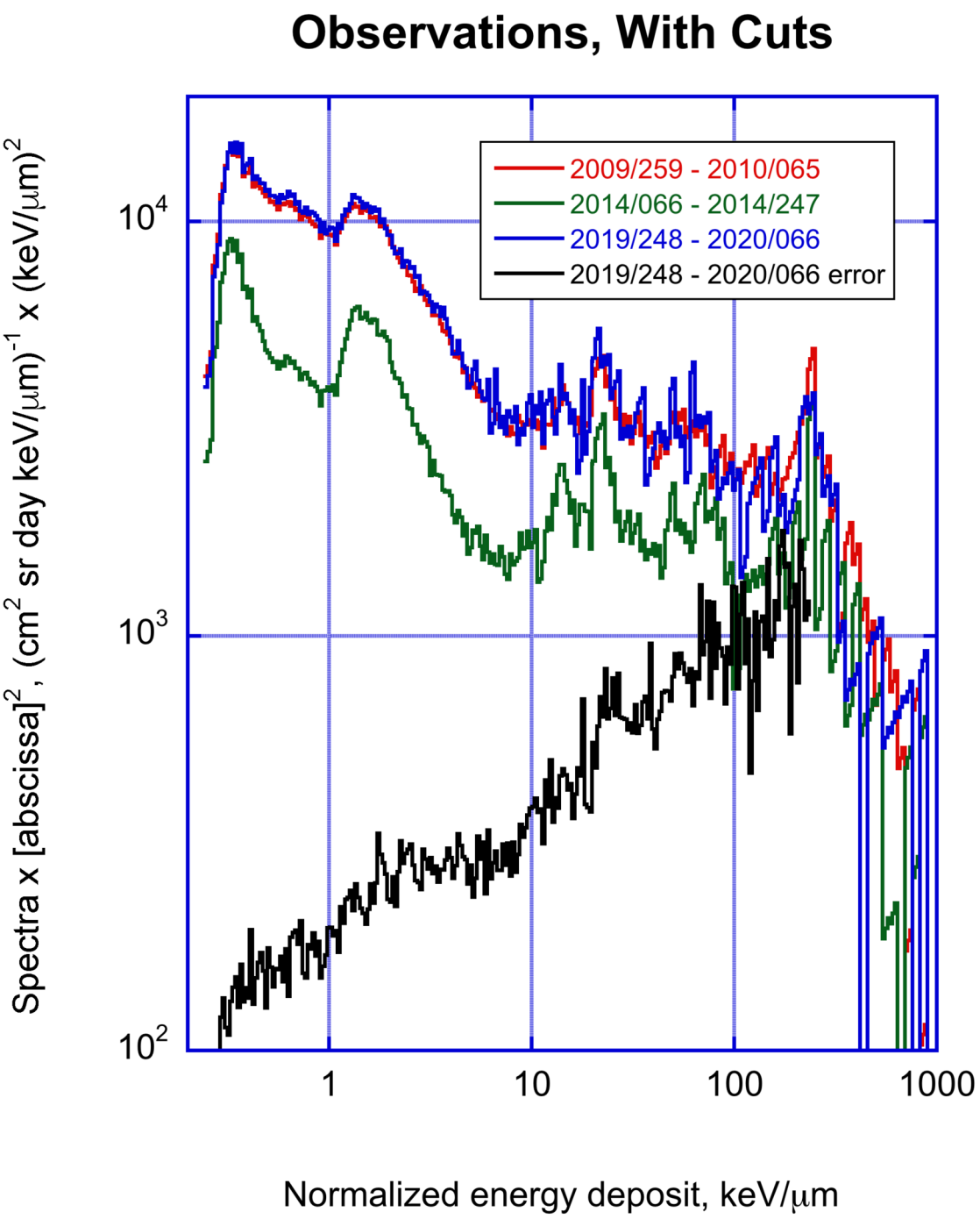

SWE_21079_2020SW002543-f07-z-.tif

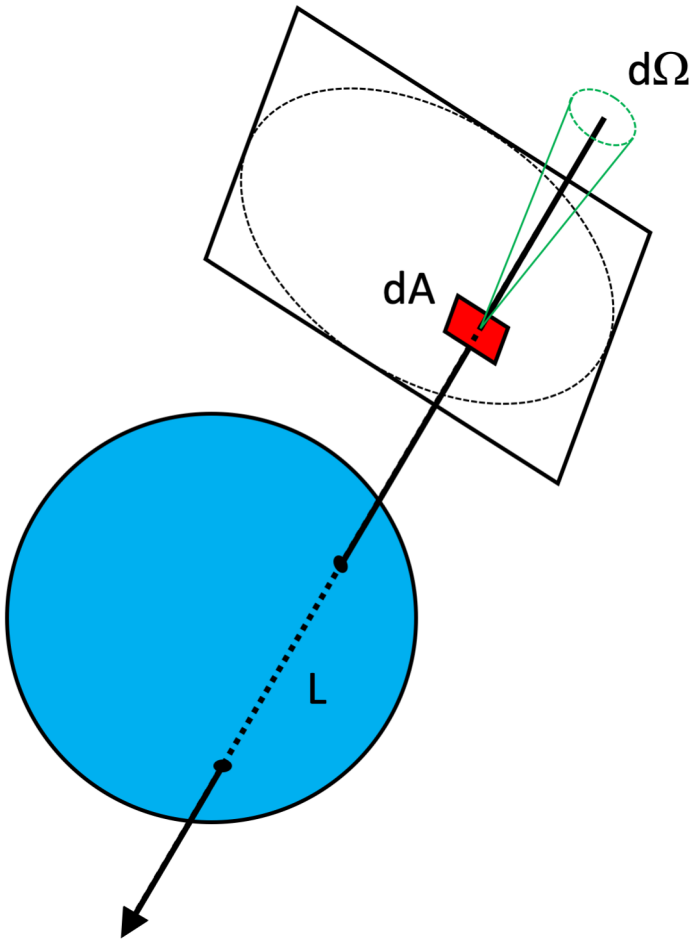

SWE_21079_2020SW002543-f08-z-.tif

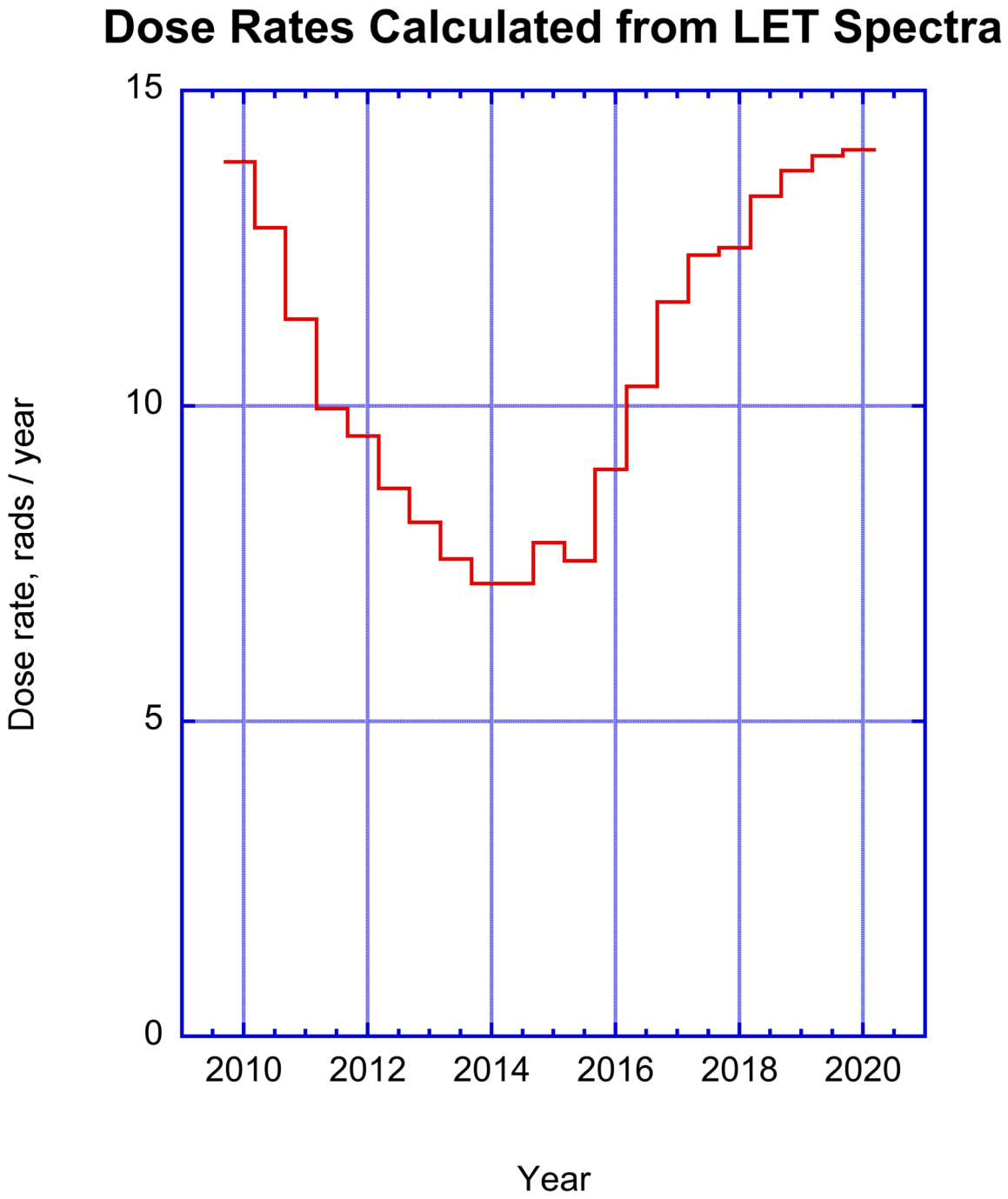

SWE_21079_2020SW002543-f09-z-.tif